Transformation of Precursor Iron(III) Minerals in Diagenetic Fluids: Potential Origin of Gray Hematite at Vera Rubin Ridge

A. L. Knight[1], K. Mitra[1]†, and J. G. Catalano[1,2]

[1]Department of Earth and Planetary Sciences, Washington University, Saint Louis, Missouri 63130, USA.

[2]McDonnell Center for the Space Sciences, Washington University, Saint Louis, Missouri 63130, USA.

Corresponding author: Abigail L. Knight (alknight@wustl.edu)

†Present Address: Department of Geosciences, Stony Brook University, Stony Brook, New York 11794, USA.

Key Points:

- Jarosite transforms to gray hematite at 200 ºC in both sulfate- and chloride-rich fluids.
- Other iron(III) minerals (goethite, akaganeite, ferrihydrite, schwertmannite, and red hematite) do not convert to gray hematite.
- Jarosite may be a viable precursor mineral to the gray hematite found at Vera Rubin ridge, Gale crater, Mars.

Abstract

Coarse-grained (> 3-5 μm) gray hematite particles occur at Vera Rubin ridge (VRR) within Gale crater, Mars. VRR has likely undergone multiple episodes of diagenesis, at least one of which resulted in the formation of gray hematite. The precursor mineralogy and nature of the diagenetic fluids that produced coarse-grained hematite remain unknown. Analog laboratory experiments were performed on a variety of iron(III) minerals to assess the potential fluid conditions and precursor mineralogy that form coarse-grained hematite. Gray hematite formed from the transformation of jarosite after 20 days at 200 ºC. Conversion was complete in chloride-rich fluids but substantial jarosite remained in sulfate-rich fluids; no transformations of jarosite occurred when aged at 98 °C. All other precursor minerals (akageneite, ferrihydrite, goethite, and schwertmannite) did not transform or produced only red, fine-grained hematite under all conditions assessed. In addition, seeding precursor iron(III) phases with red hematite and coarsening pre-existing red hematite both failed to produce gray hematite. These results suggest that jarosite was the precursor of gray hematite at VRR and the diagenetic fluids were low in sulfate and potentially chloride-rich. Jarosite produces gray hematite because the acidic conditions it generates yield both a low degree of hematite supersaturation, producing few nuclei, and high dissolved iron concentrations, enabling rapid hematite growth. Gray hematite readily forms under oxic conditions and its occurrence at VRR is not a marker for a redox interface. The associated diagenetic event was thus unlikely to have generated substantial new chemical energy for life.

Plain Language Summary

Hematite is often formed from other pre-existing iron-bearing minerals in water-rich environments. Depending on its grain size, hematite can be either red (fine-grained) or gray (coarse-grained) and these grain sizes likely indicate distinct past conditions. Gray hematite has been observed at Vera Rubin ridge (VRR) in Gale crater, Mars but how it formed is currently unknown. Laboratory experiments in this study demonstrate that jarosite, an iron- and sulfur-bearing mineral, converts to gray hematite in chloride-rich and sulfate-poor fluid conditions at elevated temperatures. Other iron(III)-bearing minerals (akageneite, ferrihydrite, goethite, schwertmannite, and fine-grained hematite) did not transform to gray hematite under any experimental conditions studied. The gray hematite at VRR likely formed by conversion from jarosite during alteration after the sediments in Gale crater had already formed. This event did not require reducing conditions and thus did not provide any new chemical energy for life.

Key words

Hematite, Jarosite, Vera Rubin ridge, Diagenesis, Gale crater, Mars

1 Introduction

Vera Rubin ridge (VRR) is a topographically-distinct sedimentary unit exposed on the northwestern slope of Aeolis Mons, the 5-km-tall central peak within Gale crater, Mars (Edgar et al., 2020). Also known as "hematite ridge," VRR has been identified as a hematite (α-Fe_2O_3)-bearing unit based on the strong ferric absorptions (attributed to the presence of crystalline hematite) throughout the ridge by both the Compact Reconnaissance Imaging Spectrometer for Mars (CRISM) onboard the Mars Reconnaissance Orbiter (MRO) and the Mars Science Laboratory (MSL) Curiosity rover (Fraeman et al., 2013; Fraeman et al., 2016; Fraeman, Johnson, et al., 2020; Johnson et al., 2016). Notably, within VRR are two separate particle sizes of hematite, each with distinct spectral characteristics (Fraeman, Johnson, et al., 2020; Horgan et al., 2020). Fine-grained hematite, also called "pigmentary hematite," is distinctly red in color but transitions to gray-colored, coarse-grained hematite at a particle size around 3-5 μm (Catling & Moore, 2003; Kerker et al., 1979; Lane et al., 2002; Morris et al., 2020). In addition to the widespread occurrences within VRR (Horgan et al., 2020), gray hematite has also been observed on Earth, such as in basaltic sediments at Maunakea volcano in Hawaii (Morris et al., 2020), Proterozoic banded iron formations (BIFs) (Fallacaro & Calvin, 2006), and sandstone injectites (Jensen et al., 2018), as well as on Mars at Meridiani Planum, Aram Chaos, and Valles Marineris (Christensen et al., 2001).

The formation of well-crystalline gray hematite rather than the more common fine-grained, red hematite in localized regions of VRR and other locations on Earth and Mars may be the result of distinct formation conditions that, in the case of VRR, are likely diagenetic (Bennett et al., 2021). VRR is composed of two hematite-bearing members of the Murray formation: the Pettegrove Point member and the Jura member (Edgar et al., 2020). Red hematite is found throughout both members, but gray hematite is primarily observed within the Jura member,

crosscutting the surrounding strata, which further supports its diagenetic origin (Horgan et al., 2020). VRR is primarily composed of thinly-laminated mudstones with distinctive diagenetic sedimentary features, including nodules, Ca sulfate veins, crystal molds, and cross-cutting color variations (Edgar et al., 2020) that are often associated with coarser-grained rock targets (Bennett et al., 2021). The mineralogy and geochemistry of VRR also provide further evidence for multiple stages of diagenetic fluid events in the past (McAdam et al., 2020; Thomas et al., 2020). The hydrogen content in samples from VRR is variable, which indicates rocks at Gale crater were possibly exposed to other aqueous activity besides that associated with a paleolake (Thomas et al., 2020). Additionally, the highest hydrogen content was frequently associated with larger grain sizes within VRR sediments which supports the argument for the formation of gray, coarse-grained hematite from fluid interactions (Thomas et al., 2020).

Compared to the recessive strata below it, VRR is also particularly resistant to weathering and maintains a distinct topographic profile, which may be the result of diagenesis (Edgar et al., 2020). Whether this increased resiliency of VRR mudstone units is due to cementation, mineralogy, or coarser grain sizes is yet to be determined. Despite substantial evidence for several past episodes of aqueous diagenesis in Gale crater (Edgar et al., 2020; Fraeman, Edgar, et al., 2020; Frydenvang et al., 2017; Horgan et al., 2020; Stack et al., 2014; Thomson et al., 2011), the origin and nature of the permeating fluids, as well as the precursor mineralogy, remain unclear. Diagenetic fluid temperatures, acidities, salinities, and compositions are not well-constrained for VRR. Identifying candidate minerals and the range of possible fluid conditions that generate gray hematite provides insight into past diagenetic events and the potential for ancient habitable conditions at Gale crater.

The purpose of this study is to investigate the transformation products of iron(III) minerals subjected to simulated diagenetic fluid conditions and identify potential pathways to gray hematite. Iron(III) minerals were aged in a variety of Mars-relevant fluids to assess the impact of variable initial pH values, background salts, and temperatures on the reaction products formed. Mineralogy and crystallinity of the solid transformation products were determined, including identification via grain size-dependent spectral features in the visible wavelengths. This study provides a broad assessment of potential precursors to well-crystalline hematite that are either directly observed on Mars or expected to occur given its geologic history.

2 Methods

2.1 Precursor mineral synthesis

Akaganeite (β-$FeO_{1-x}(OH)_{1+x}Cl_x$), ferrihydrite (~$Fe_{10}O_{14}(OH)_2 \cdot nH_2O$), goethite ($\alpha$-FeOOH), ~60 nm red hematite, ~10 nm red hematite, schwertmannite ($Fe_8O_8(OH)_{8-x}(SO_4)_x \cdot nH_2O$), and potassium jarosite ($KFe_3(SO_4)_2(OH)_6$) were synthesized according to standard laboratory techniques (see supporting information for full details). It was necessary to produce multiple batches for some experiments due to constraints on the mass of mineral produced in each synthesis. Each synthesized mineral was washed, dried in a convection oven at ~40 ºC (ferrihydrite was dried in a desiccator instead of by heating because of its instability at elevated temperatures), and ground to a powder in a mortar and pestle. The mineralogical purity of each synthesis product was evaluated via powder X-ray diffraction (XRD).

2.2 Simulated diagenesis experiments

Laboratory experiments were performed to approximate potential conditions under which precursor iron(III) minerals (akageneite, ferrihydrite, goethite, red hematite, jarosite, and

schwertmannite) may transform (or coarsen) diagenetically to gray, coarse-grained hematite in an aqueous setting. For each initial mineral, ~1.6 to 2 g were suspended in ultrapure water and added to a salt solution containing either magnesium chloride or magnesium sulfate to create a 20 mL mineral suspension; chloride and sulfate salts have been observed throughout VRR via Sample Analysis at Mars (SAM) and Chemistry and Mineralogy (CheMin) analyses (Clark et al., 2020; McAdam et al., 2020; Rampe et al., 2020). Total salt concentrations in final solutions were set to 1 mol L^{-1}. Additional experiments on goethite and ferrihydrite were conducted with small amounts of ~60 nm hematite added to seed the transformations. A 1:9 molar ratio of hematite to goethite or ferrihydrite was added, assuming chemical formulas of α-FeOOH and $Fe_{10}O_{14}(OH)_2$ for goethite and ferrihydrite, respectively. Each 20 mL mineral suspension was adjusted to a pH value of either 3 or 7 via dropwise additions of 1 mol L^{-1} hydrochloric acid and 1 mol L^{-1} sodium hydroxide. Since jarosite has the ability to generate substantial acidity through the release of H^+ as it dissolves and reacts quickly with added base, the solution pH was set before adding this mineral and the pH then freely evolved during reaction. Additional jarosite experiments used 0.1 mol L^{-1} salt concentrations to investigate the impact of different anion concentrations. The resulting mineral suspensions were heated in a digital convection oven for 20 days at 98 ºC in polypropylene tubes sealed with PTFE thread seal tape or 200 ºC in PTFE-lined bombs (Parr Instrument Co.) to minimize fluid vaporization; the 98°C experiments resulted in ~20-30% evaporative loss of the solution.

2.3 Mineral and fluid characterization

After aging for 20 days at elevated temperatures, the experiments were ended and the sample products were cooled to room temperature. The resulting suspensions were passed through 0.22 µm mixed cellulose ester (MCE) filters via syringe filtration to isolate the fluids from the

solid product. The final pH values of the fluids were measured, and final dissolved iron (as well as potassium and sulfur for experiments involving jarosite) concentrations were determined via inductively-coupled plasma optical emission spectrometry (ICP-OES) using a Thermo iCap 7400 Duo instrument. Each fluid sample was measured 3 times, and the raw counts were averaged. The uncertainties in the slope and intercept of the calibration curves, obtained by linear regression, were propagated with the standard deviations of the measurements reported by the instrument to obtain concentration errors.

The solid products were washed with ultrapure water either via syringe filtration, vacuum filtration, or centrifugation to remove residual salts, dried in a convection oven, and ground with a mortar and pestle. The powdered mineral products were then analyzed via powder XRD and visible to near infrared (VNIR) reflectance spectroscopy. VNIR spectroscopy was performed on the solid transformation products using an Analytical Spectral Devices (ASDs) portable VNIR spectroradiometer to identify key absorption features. The resulting spectra were splice-corrected to reduce the offsets at ~1000 and ~1825 nm between each of the three built-in detectors. Powder XRD was performed using a Bruker d8 Advance powder X-ray diffractometer, Cu X-ray source (40 kV and 40 mA), step size of 0.02° per step, and counting time of 0.5 seconds per step for each measurement. A LynxEye XE energy-dispersive strip detector was used for data collection. Each of the 192 detector strips separately measures a given 2θ value for the stated counting time, giving a total integration time per point of 96 s. Final mineral abundances and coherent scattering domain sizes were determined using Profex to perform Rietveld refinement on the XRD patterns (Doebelin & Kleeberg, 2015).

For samples with a coherent scattering domain (CSD) size greater than ~100 to 200 nm, the peak width is determined by instrumental broadening rather than the actual domain size.

Therefore, select samples with large CSD sizes were imaged with a Thermofisher Quattro S Scanning Electron Microscope (SEM) to examine both the morphology and particle size of the solid products. CSD size indicates the size within an individual crystallite where atomic structure is uniform and X-rays are scattered coherently, whereas particle size refers to the visual size of discreet grains, which may be agglomerates of smaller crystals. When particles are single crystals and not aggregates, the CSD size is equal to the particle size. The SEM images were analyzed using ImageJ (Schneider et al., 2012) to measure individual particle sizes. The measured particle sizes taken from the SEM images may be biased toward grains that are larger, intact, and unobscured by other surrounding particles because they are more visible in an image.

3 Results

3.1 Characterization of precursor minerals

All synthesized precursor minerals were free of other phases and generally showed consistent particle sizes among different batches (Table S1). The two batches of goethite used in the single-mineral experiments resulted in multi-domainic acicular needles generally about 2 to 4 μm long and 0.1 to 0.4 μm wide (Table S1; Figures S1 and S2). The third batch of goethite, synthesized for the two-mineral experiments, had a slightly smaller coherent domain size based on refinement of its diffraction pattern (Table S1; Figure S3). Synthesized akaganeite (Figure S4) resulted in a CSD size of 15 ± 1 nm based on refinement of its XRD pattern (Table S1; Figure S5). Two batches of ferrihydrite were synthesized for the single-mineral and two-mineral experiments. Both batches had two broad diffraction peaks (Figures S6 and S7), indicative of two-line ferrihydrite, which typically consists of crystallites 2 to 3 nm in size (Janney et al., 2000; Michel et al., 2007). Note that crystallite size cannot be determined using XRD patterns for particles smaller ~10 nm because of the lack of long-range periodicity (Egami & Billinge, 2012). The initial

schwertmannite produced a diffraction pattern with broad peaks (Figure S8), consistent with a particle size of < 10 nm. Two batches of red hematite with ~60 nm CSD sizes were synthesized, one for the single-mineral experiments and one for the two-mineral experiments where goethite and ferrihydrite were seeded with hematite (Table S1; Figure S9). A final batch of red hematite with ~10 nm CSD size was synthesized for the single-mineral experiments to explore the impact of the initial hematite particle size on the transformation products (Table S1; Figure S10). The jarosite synthesized had an initial crystallite size of 89 ± 4 nm (Table S1).

3.2 Transformation of individual precursor minerals

3.2.1 Product mineralogy

The transformation products of experiments performed on individual precursor minerals were identified via XRD. Hematite was the most common reaction product from the iron(III) minerals assessed (Table 1). Diffraction patterns indicate that hematite (both ~10 nm and ~60 nm), akaganeite, ferrihydrite, and schwertmannite fully converted to (or remained) crystalline hematite in experiments performed at 200 ºC (Figure 1; Table 1; Figures S5, S6, and S8-S10). However, goethite and jarosite resulted in more variable reaction products (Tables 1 and 2; Figures 1 and 2; see Figure S2 for all goethite patterns). Goethite transformed to red hematite at a higher temperature under acidic conditions but resulted in a mixture of red hematite and goethite at pH 7 and 200 ºC (Table 1; Figure 2; Figure S2). Experiments on jarosite at high temperatures (200 ºC) yielded mixtures of hematite and jarosite in sulfate fluids and 0.1 mol L^{-1} chloride fluids, while complete transformation to crystalline hematite occurred in 1 mol L^{-1} chloride fluids (Table 2; Figures 1 and 2). Diffraction patterns indicate that hematite (both ~10 nm and ~60 nm), akaganeite, and ferrihydrite typically transformed completely to or remained crystalline hematite in experiments performed at 98 ºC (Table 1; see Figures S5, S6, S9, and S10 for all patterns). Goethite

and jarosite did not show evidence of transformation at 98 ºC (Tables 1 and 2; Figures 1 and 2), but schwertmannite completely converted to goethite at this temperature (Figure S8).

Table 1. Final mineral abundances, crystallite sizes, and particle sizes of the solid products of experiments on the transformation of akageneite, ferrihydrite (seeded and unseeded), goethite (seeded and unseeded), hematite (~10 nm and ~60 nm), and schwertmannite in simulated diagenetic fluids.

Initial Mineral	Temperature (°C)	Salt	Initial pH	Final Mineral Abundances (wt. %)		Crystallite Size (nm)		Particle Size (nm)
				Hematite	*Akaganeite*	*Hematite*	*Akaganeite*	*Hematite*
akaganeite	98	1 mol L^{-1} $MgCl_2$	3	100	-	35 ± 1	-	-
			7	100	-	45 ± 2	-	-
		1 mol L^{-1} $MgSO_4$	3	100	-	16.7 ± 0.5	-	-
			7	70 ± 2	30 ± 2	24 ± 1	3.6 ± 0.4	-
	200	1 mol L^{-1} $MgCl_2$	3	100	-	66 ± 2	-	600 ± 200
			7	100	-	63 ± 2	-	-
		1 mol L^{-1} $MgSO_4$	3	100	-	60 ± 2	-	-
			7	100	-	64 ± 2	-	-
				Hematite		*Hematite*		
ferrihydrite	98	1 mol L^{-1} $MgCl_2$	3	100		87 ± 2		-
			7	100		73 ± 2		-
		1 mol L^{-1} $MgSO_4$	3	100		62 ± 2		-
			7	100		77 ± 2		-
	200	1 mol L^{-1} $MgCl_2$	3	100		79 ± 3		90 ± 20
			7	100		72 ± 2		-
		1 mol L^{-1} $MgSO_4$	3	100		65 ± 2		-
			7	100		57 ± 1		-
				Hematite	*Goethite*	*Hematite*	*Goethite*	
goethite	98	1 mol L^{-1} $MgCl_2$	3	-	100	-	47 ± 1	-
			7	-	100	-	46 ± 1	-
		1 mol L^{-1} $MgSO_4$	3	-	100	-	47 ± 1	-
			7	-	100	-	48 ± 1	-
	200	1 mol L^{-1} $MgCl_2$	3	100	-	240 ± 7	-	1000 ± 500
			7	1.9 ± 0.5	98.1 ± 0.5	68 ± 40	52 ± 1	-
		1 mol L^{-1} $MgSO_4$	3	97.2 ± 0.5	2.8 ± 0.5	220 ± 7	60 ± 10	-
			7	43.7 ± 0.6	56.3 ± 0.6	206 ± 9	62 ± 2	-
				Hematite		*Hematite*		
hematite (~10 nm)	98	1 mol L^{-1} $MgCl_2$	3	100		22.5 ± 0.6		-
			7	100		22.7 ± 0.7		-
		1 mol L^{-1} $MgSO_4$	3	100		20.1 ± 0.5		-
			7	100		19.6 ± 0.5		-
	200	1 mol L^{-1} $MgCl_2$	3	100		37 ± 1		50 ± 20

			7	100		32.8 ± 0.9	-
		1 mol L^{-1} $MgSO_4$	3	100		35 ± 1	-
			7	100		34.6 ± 1.0	-
				Hematite		*Hematite*	
hematite (~60 nm)	98	1 mol L^{-1} $MgCl_2$	3	100		58 ± 1	-
			7	100		57 ± 1	-
		1 mol L^{-1} $MgSO_4$	3	100		56 ± 1	-
			7	100		55 ± 1	-
	200	1 mol L^{-1} $MgCl_2$	3	100		64 ± 2	90 ± 20
			7	100		60 ± 2	-
		1 mol L^{-1} $MgSO_4$	3	100		64 ± 2	-
			7	100		63 ± 1	-
				Hematite	*Goethite*	*Hematite*	*Goethite*
schwertmannite	98	1 mol L^{-1} $MgCl_2$	3	-	100	-	13.1 ± 0.4
			7	-	100	-	13.5 ± 0.5
		1 mol L^{-1} $MgSO_4$	3	-	100	-	14 ± 1
			7	-	100	-	14.7 ± 0.4
	200	1 mol L^{-1} $MgCl_2$	3	100	-	133 ± 4	-
			7	100	-	109 ± 4	-
		1 mol L^{-1} $MgSO_4$	3	100	-	97 ± 4	-
			7	100	-	81 ± 5	-
				Hematite		*Hematite*	
	98	1 mol L^{-1} $MgCl_2$	3	100		93 ± 2	-
			7	100		68 ± 2	-
		1 mol L^{-1} $MgSO_4$	3	100		45 ± 2	-
ferrihydrite			7	100		70 ± 2	-
seeded with hematite	200	1 mol L^{-1} $MgCl_2$	3	100		99 ± 2	120 ± 30
			7	100		65 ± 2	-
		1 mol L^{-1} $MgSO_4$	3	100		83 ± 2	-
			7	100		61 ± 1	-
				Hematite	*Goethite*	*Hematite*	*Goethite*
	98	1 mol L^{-1} $MgCl_2$	3	18.0 ± 0.9	82.0 ± 0.9	64 ± 6	37 ± 1	-
			7	15.5 ± 0.8	84.5 ± 0.8	64 ± 7	27.5 ± 0.7	-
		1 mol L^{-1} $MgSO_4$	3	12 ± 1	88 ± 1	50 ± 10	26.4 ± 0.9	-
goethite			7	17.9 ± 0.7	82.1 ± 0.7	57 ± 5	32.2 ± 0.8	-
seeded with hematite	200	1 mol L^{-1} $MgCl_2$	3	100	-	158 ± 4	-	240 ± 90
			7	15 ± 1	85 ± 1	58 ± 9	32 ± 1	-
		1 mol L^{-1} $MgSO_4$	3	100	-	143 ± 4	-	-
			7	32.3 ± 0.8	67.7 ± 0.8	80 ± 4	35.7 ± 1.0	-

228 **Table 2.** Final mineral abundances, crystallite sizes, and particle sizes of the solid products of experiments on the transformation of
229 jarosite in simulated diagenetic fluids.
230

Initial Mineral	Temperature (°C)	Salt	Initial pH	Final Mineral Abundances (wt. %)		Crystallite Size (nm)		Particle Size (nm)
				Hematite	*Jarosite*	*Hematite*	*Jarosite*	*Hematite*
jarosite	98	0.1 mol L^{-1} $MgCl_2$	3	-	100	-	163 ± 5	-
			7	-	100	-	148 ± 5	-
		0.1 mol L^{-1} $MgSO_4$	3	-	100	-	128 ± 4	-
			7	-	100	-	119 ± 3	-
	200	0.1 mol L^{-1} $MgCl_2$	3	67.1 ± 0.7	32.9 ± 0.7	128 ± 5	55 ± 3	6000 ± 1000
			7	64.4 ± 0.7	35.6 ± 0.7	150 ± 5	58 ± 3	-
		0.1 mol L^{-1} $MgSO_4$	3	72.9 ± 0.7	27.1 ± 0.7	181 ± 7	67 ± 4	6000 ± 1000
			7	70.9 ± 0.6	29.1 ± 0.6	223 ± 9	92 ± 5	-
	98	1 mol L^{-1} $MgCl_2$	3	-	100	-	220 ± 8	-
			7	-	100	-	210 ± 7	-
		1 mol L^{-1} $MgSO_4$	3	-	100	-	106 ± 3	-
			7	-	100	-	104 ± 3	-
	200	1 mol L^{-1} $MgCl_2$	3	100.00	-	290 ± 20	-	14000 ± 4000
			7	100.00	-	300 ± 10	-	-
		1 mol L^{-1} $MgSO_4$	3	12.3 ± 0.5	87.8 ± 0.5	340 ± 50	210 ± 10	2000 ± 1000
			7	19 ± 1	81 ± 1	270 ± 60	120 ± 10	-

231

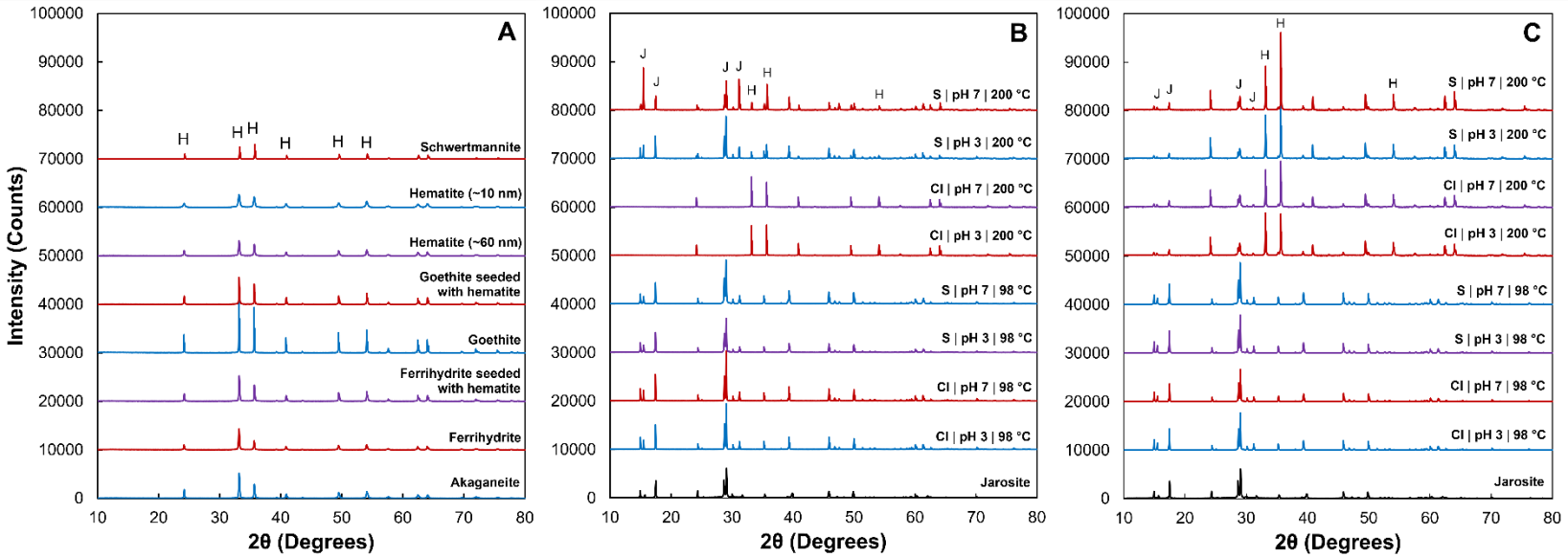

Figure 1. XRD patterns of (a) the red hematite transformation products of synthesized minerals subjected to pH 3, 1 mol L^{-1} $MgCl_2$ 200 ºC fluid conditions for 20 days, (b) synthesized jarosite and its transformation products in various 1 mol L^{-1} fluid conditions, and (c) synthesized jarosite and its transformation products in various 0.1 mol L^{-1} fluid conditions. Cl and S indicate $MgCl_2$ and $MgSO_4$ background salts, respectively, in the transformation fluids. Initial fluid pH value (pH 3 or pH 7) and experimental temperature (98 ºC or 200 ºC) are indicated for each sample. Characteristic jarosite ("J") and hematite ("H") peaks are labeled. Patterns offset in intervals of 10000 and patterns from experiments on jarosite in 200 ºC fluids with 0.1 mol L^{-1} salt vertically exaggerated by a factor of 2 for clarity.

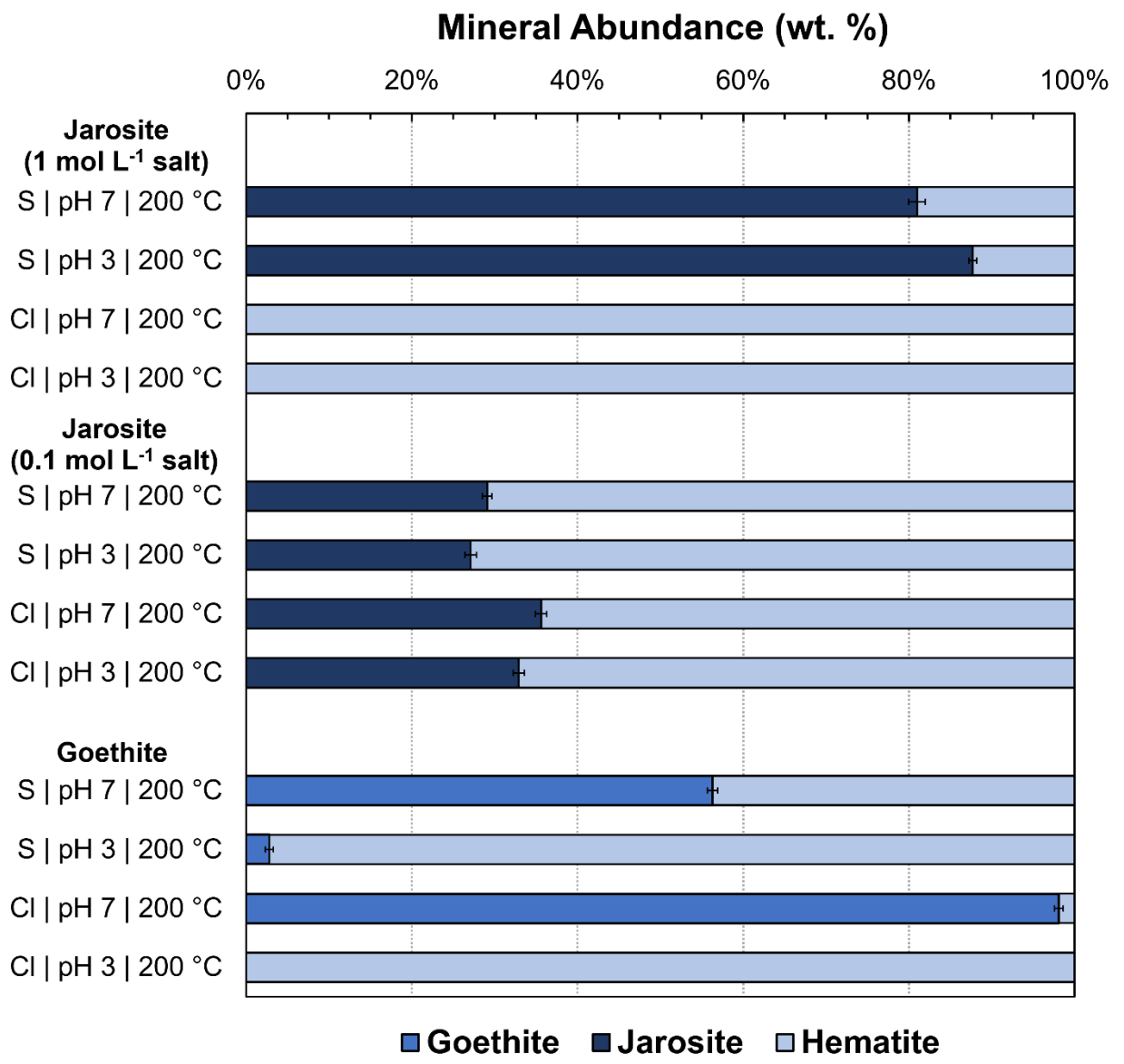

Figure 2. Final mineralogy (wt.%) of reaction products of jarosite and goethite experiments. Cl and S indicate background salts of $MgCl_2$ and $MgSO_4$, respectively, in the transformation fluids. Initial fluid pH value (pH 3 or pH 7) and experimental temperature (200 ºC) are provided for each sample.

3.2.2 Fluid composition

In general, experiments on akageneite, ferrihydrite, schwertmannite, ~10 nm red hematite, and jarosite produced substantial (> 1 pH unit) decreases in pH value (Table 3; Table S2). The final pH values of ~60 nm hematite and goethite fluids remained relatively unchanged from the initial value in comparison. Across all experiments, final pH values tended to be higher for sulfate-rich samples and lower for chloride-rich samples (Table 3; Table S2). We attribute the decrease in pH to fluid evaporation and grain coarsening. The latter process decreases total surface area in the system, releasing H^+ as anions desorb and surface sites are overgrown. Schwertmannite, akaganeite, and jarosite also generate H^+ as they transform to hematite.

Jarosite experiments displayed final dissolved concentrations of iron, potassium, and sulfur that were non-stoichiometric with respect to the chemical formula of potassium jarosite (Table 3). Jarosite partially dissolved when aged at 98 ºC (Table 3) but no new phases were precipitated (Table 2; Figures 1 and 2). The final fluid compositions in these samples are therefore only controlled by the dissolution of jarosite. In the samples where jarosite was the sole mineral phase present at the end of the experiment, iron was substantially depleted in the final fluid composition relative to both sulfur and potassium, while potassium was enriched slightly relative to sulfur. In addition, elevated chloride concentrations increased the ratio of iron to sulfur and decreased the ratio of iron to potassium in the final fluid (Table 3).

265 **Table 3.** Final fluid compositions (pH values, dissolved ion concentrations, and molar ratios) of experiments on the transformation of
266 jarosite in simulated diagenetic fluids.
267

Temperature (°C)	Salt	Initial pH	Final pH	Fe (mmol/kg)	K (mmol/kg)	S (mmol/kg)	K:S	K:Fe
98	0.1 mol L^{-1} $MgCl_2$	3	1.46	0.338 ± 0.004	52.6 ± 0.6	66 ± 3	0.79 ± 0.04	156 ± 3
		7	1.48	0.36 ± 0.004	60.1 ± 0.4	72 ± 3	0.84 ± 0.04	167 ± 2
	0.1 mol L^{-1} $MgSO_4$	3	1.75	0.109 ± 0.002	35.7 ± 0.6	-	-	326 ± 9
		7	1.47	0.095 ± 0.002	39.4 ± 0.4	-	-	415 ± 10
200	0.1 mol L^{-1} $MgCl_2$	3	1.12	2.2 ± 0.04	147.9 ± 0.8	260 ± 4	0.568 ± 0.008	67 ± 1
		7	1.11	2.2 ± 0.04	176.3 ± 0.9	275 ± 5	0.64 ± 0.01	80 ± 1
	0.1 mol L^{-1} $MgSO_4$	3	0.78	0.71 ± 0.03	136 ± 1	-	-	193 ± 10
		7	0.72	0.96 ± 0.03	185.5 ± 0.9	-	-	194 ± 7
98	1 mol L^{-1} $MgCl_2$	3	0.84	11.97 ± 0.09	66.3± 0.4	93 ± 3	0.71 ± 0.02	5.54 ± 0.06
		7	0.90	12.4 ± 0.1	58.3 ± 0.4	91 ± 3	0.64 ± 0.02	4.70 ± 0.05
	1 mol L^{-1} $MgSO_4$	3	1.87	0.232 ± 0.003	38.3 ± 0.4	-	-	165 ± 3
		7	1.55	0.109 ± 0.002	39 ± 0.4	-	-	359 ± 8
200	1 mol L^{-1} $MgCl_2$	3	0.52	60.9 ± 0.6	213 ± 2	353 ± 4	0.603 ± 0.008	3.50 ± 0.04
		7	0.43	75 ± 2	180 ± 1	393 ± 4	0.459 ± 0.006	2.40 ± 0.08
	1 mol L^{-1} $MgSO_4$	3	1.01	0.203 ± 0.003	83.2 ± 0.8	-	-	410 ± 7
		7	0.89	0.314 ± 0.004	133 ± 1	-	-	423 ± 6

268
269

3.2.3 Particle and crystallite sizes

Generally, high temperature (200 ºC), chloride-rich, acidic conditions produced the largest final CSD sizes of hematite for most minerals. Refinement of diffraction patterns for the hematite reaction products of ~10 nm red hematite, ~60 nm red hematite, akaganeite, ferrihydrite, and schwertmannite resulted in CSD sizes generally less than 150 nm (Table 1), indicative of red hematite. Initial hematite with a smaller, ~10 nm initial CSD size experienced a greater relative increase in size compared to larger, ~60 nm initial hematite but its final particle size was still smaller than that of the ~60 nm hematite. The XRD-derived CSD sizes of the hematite produced from precursor akageneite were < 70 nm; however, SEM images show 0.6 ± 0.2 µm particles, suggesting that these particles were aggregates of multiple individual crystals (Figures 3 and 4).

In contrast, goethite and jarosite generally resulted in more crystalline hematite reaction products with crystallite sizes that exceeded the upper limit of quantification from XRD patterns (Tables 1 and 2). SEM images revealed that goethite in acidic, high temperature (200 ºC) fluids converted to hematite with a particle size of ~1 µm (Figures 3 and 4). SEM images of the hematite produced from jarosite show that in chloride-rich, 200 ºC fluids, hematite ranged in length from ~5-20 µm (Figures 4 and 5). In fluids with lower (0.1 mol L^{-1}) chloride concentrations and fluids with sulfate, the hematite product of jarosite was smaller (< 10 µm) but still notably coarse (Figures 4 and 5). The morphology of the hematite product varied with grain size (Figures 3 and 5; Figure S11). Small (~1 µm) particles were rhombohedral, while larger (~14 µm long) particles were elongated and somewhat “spindle-shaped,” with distinct crystal faces.

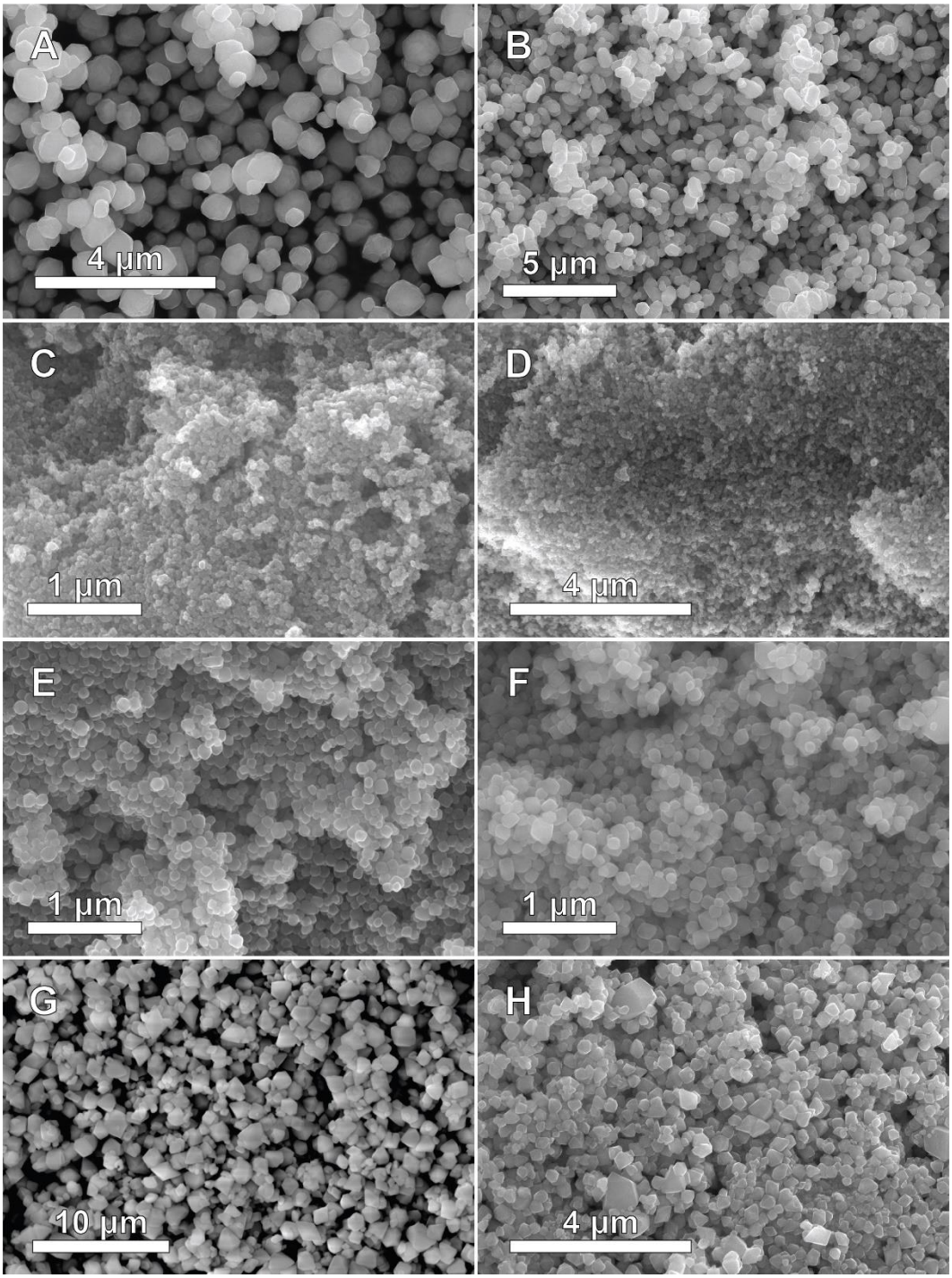

Figure 3. SEM images of the red hematite transformation products of synthesized minerals subjected to 1 mol L^{-1} $MgCl_2$, pH 3, 200 ºC fluids for 20 days. Initial mineralogy: (a) akageneite, (b) schwertmannite, (c) hematite batch 3 (~10 nm), (d) hematite batch 1 (~60 nm), (e) ferrihydrite batch 1, (f) ferrihydrite batch 2 seeded with hematite batch 2, (g) goethite batch 2, (h) goethite batch 3 seeded with hematite batch 2.

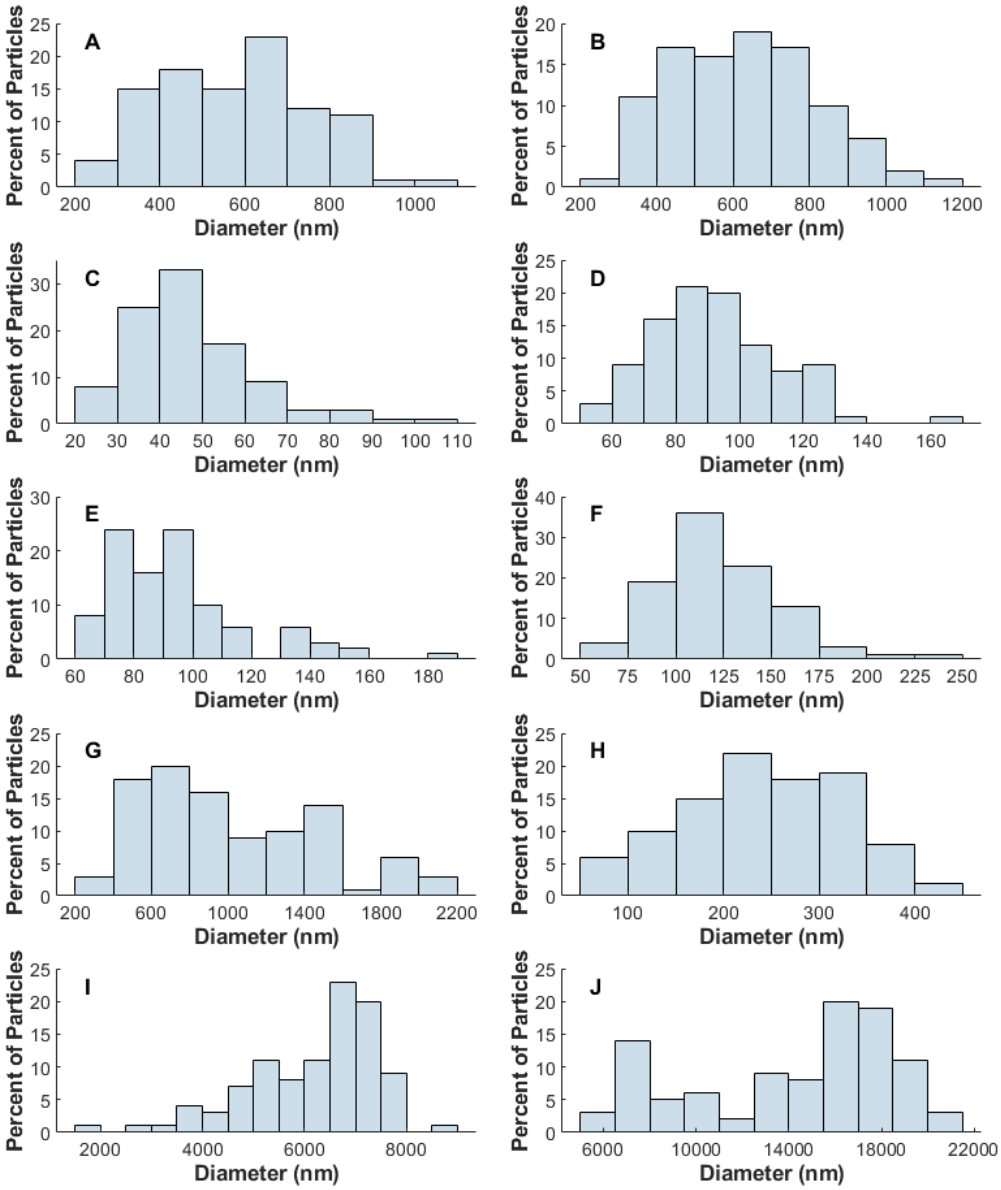

Figure 4. Measured final particle sizes of the hematite transformation products of (a) akageneite, (b) schwertmannite, (c) hematite batch 3 (~10 nm), (d) hematite batch 1 (~60 nm), (e) ferrihydrite batch 1, (f) ferrihydrite batch 2 seeded with hematite batch 2, (g) goethite batch 2, and (h) goethite batch 3 seeded with hematite batch 2 subjected to pH 3, 1 mol L^{-1} $MgCl_2$, 200 ºC fluids for 20 days. Measured final particle sizes of the hematite transformation products of jarosite subjected to (i) 0.1 mol L^{-1} $MgCl_2$ and (j) 1 mol L^{-1} $MgCl_2$ fluids set to pH 3 and heated to 200 ºC for 20 days.

304

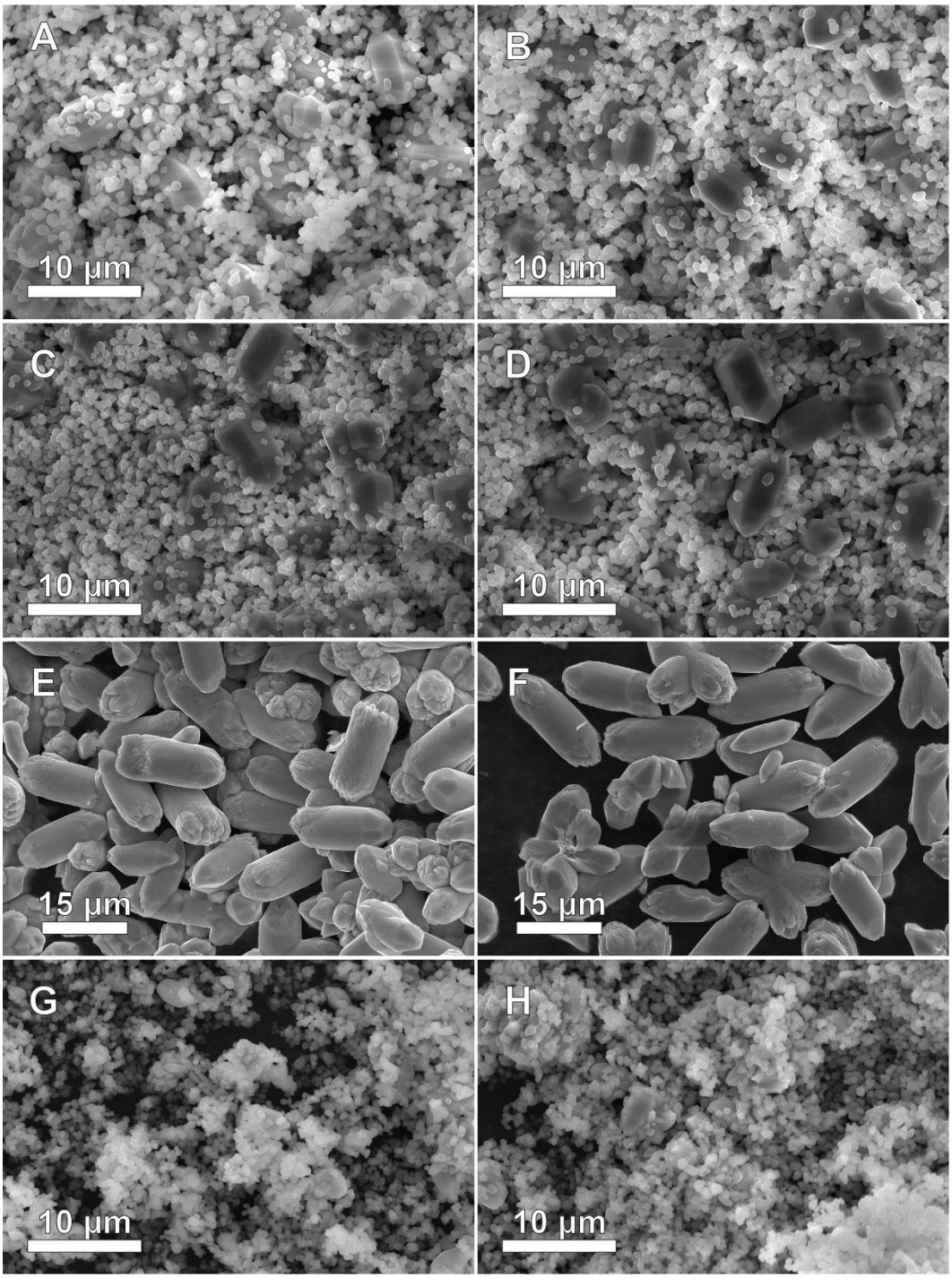

305

306 **Figure 5.** SEM images of the transformation products of jarosite subjected to various 200 ºC
307 fluids for 20 days. Fluid characteristics: (a) pH 3, 0.1 mol L^{-1} $MgCl_2$ (b) pH 7, 0.1 mol L^{-1} $MgCl_2$,
308 (c) pH 3, 0.1 mol L^{-1} $MgSO_4$, (d) pH 7, 0.1 mol L^{-1} $MgSO_4$, (e) pH 3, 1 mol L^{-1} $MgCl_2$, (f) pH 7,
309 1 mol L^{-1} $MgCl_2$, (g) pH 3, 1 mol L^{-1} $MgSO_4$, (h) pH 7, 1 mol L^{-1} $MgSO_4$.

3.2.4 Reflectance spectroscopy

Hematite and other iron (oxyhydr)oxides are identifiable via visible to near-infrared (VNIR) reflectance spectroscopy due to four electronic absorption features occurring between 400 and 1000 nm (Sherman, 1985). These electronic absorptions are visible when the iron (oxyhydr)oxide is both crystalline and maintains a small enough particle size that it retains a strong positive reflectance slope in the red portion of the visible spectrum (Lane et al., 2002). Distinguishing between different iron (oxyhydr)oxides can be challenging because the key absorption features often overlap (Catling & Moore, 2003; Morris et al., 2000). However, red, fine-grained hematite and gray, coarse-grained hematite can be distinguished easily from each other and from other iron (oxyhydr)oxides. Fine-grained hematite has a strong 860 nm absorption feature similar to other ferric minerals but exhibits a sharper inflection at 535 nm (Fraeman, Johnson, et al., 2020; Lane et al., 2002; Morris et al., 2000; Sherman & Waite, 1985). Coarse-grained hematite has strong absorption at all visible wavelengths, eliminating the 535 nm inflection and 860 nm ferric absorption edge from its visible spectrum and producing a "flat" or neutral reflectance spectrum at all visible wavelengths (Lane et al., 2002; Morris et al., 2020).

Transformation products of most minerals exhibited the 860 nm electronic absorption feature as well as the spectral inflection at 535 nm characteristic of red crystalline hematite with VNIR spectroscopy (Figure 6; Figures S12-S18). The large grain size of the hematite particles produced from interaction of jarosite with chloride-rich, 200 ºC fluids is supported by the VNIR spectra (Figure 6; Figures S19 and S20). These spectra exhibit decreased reflectance in the red portion of the visible spectrum, causing them to be more spectrally neutral, a characteristic of gray hematite. Reaction products that contain mixtures of hematite and jarosite (e.g., sulfate-rich samples) exhibit jarosite absorption features at ~435 nm and have "flatter" slopes and less

reflectance in the visible portion of the spectrum compared to that of pure jarosite (Figure 6; Figures S19 and S20).

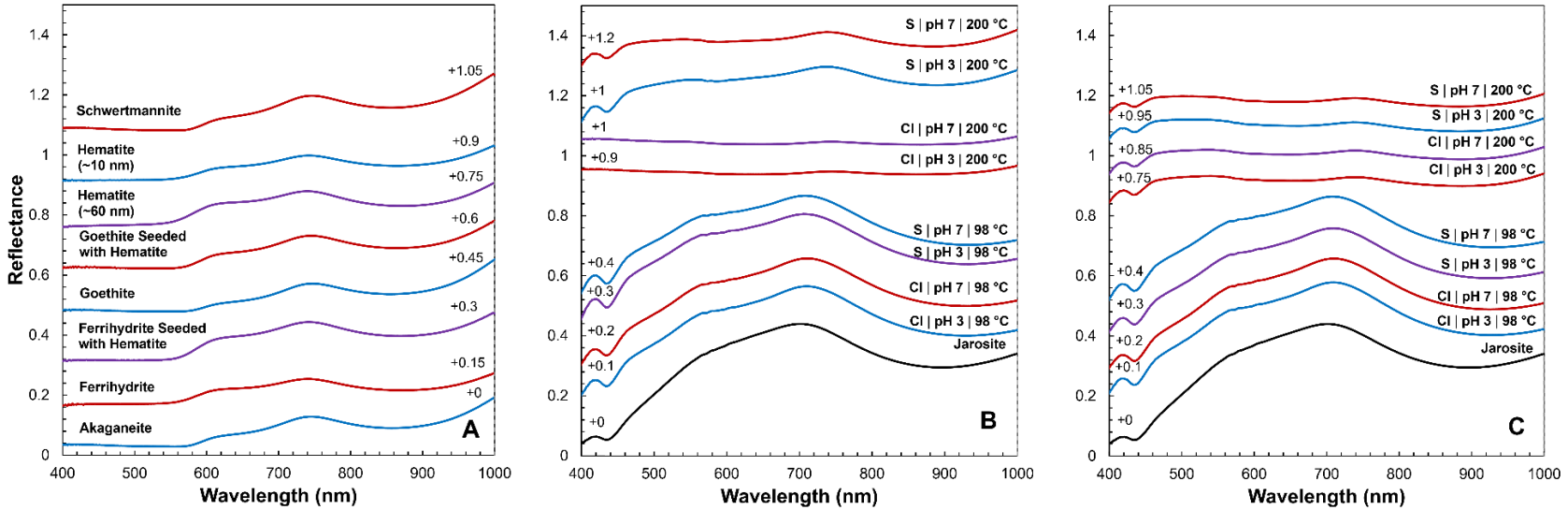

Figure 6. VNIR reflectance spectra of (a) red hematite transformation products of synthesized minerals subjected to pH 3, 1 mol L^{-1} $MgCl_2$, 200 ºC fluid conditions for 20 days, (b) synthesized jarosite and its transformation products in various 1 mol L^{-1} fluid conditions and (c) synthesized jarosite and its transformation products in various 0.1 mol L^{-1} fluid conditions. Cl and S indicate background salts of $MgCl_2$ and $MgSO_4$, respectively, in the transformation fluids. Initial fluid pH value (pH 3 or pH 7) and experimental temperature (98 ºC or 200 ºC) are provided for each sample. Spectra offset for clarity as indicated.

3.3 Effect of hematite seeds on precursor mineral transformations

Additional experiments involving goethite or ferrihydrite seeded with hematite produced similar results as the experiments which investigated goethite or ferrihydrite alone. Complete conversion of the goethite mineral mixture to hematite resulted from high temperature, acidic conditions (Figure 1; Figure S3), whereas ferrihydrite seeded with hematite completely converted to hematite in all conditions (Figure 1; Figure S7). Final hematite particle sizes for all experiments seeded with hematite were substantially smaller than the 3 to 5 μm minimum size of gray hematite (Table 1; Figures 3 and 4; Figures S3 and S7) and produced spectra consistent with red hematite (Figures S21 and S22).

4 Discussion

4.1 Impacts of precursor mineralogy on hematite transformation products

4.1.1 Jarosite

Jarosite was the only initial mineral to yield gray, crystalline hematite in the transformation products of any experimental conditions. Prior studies (e.g., Golden et al. (2008)) have produced μm-scale rounded hematite particles from hydronium jarosite, which further emphasizes that crystalline hematite can be formed from jarosite. Similar to all other initial minerals, experiments on jarosite in chloride-rich, high temperature (200 ºC), acidic fluid conditions generally resulted in the largest average hematite grain size post-transformation. The detection of tridymite at Gale crater implies the past existence of hydrothermal fluids in the crater (Yen et al., 2021), which would have promoted the formation of larger hematite. Jarosite proved to be more stable in sulfate-rich fluids than in chloride-rich fluids, as anticipated, due to the common ion effect. Increased

stability of jarosite in sulfate solutions resulted in only partial transformation to hematite in most higher temperature (200 ºC) experiments for both 1 mol L^{-1} and 0.1 mol L^{-1} sulfate concentrations.

Diffraction patterns of the final solid products of experiments on jarosite at 98 ºC indicated that no secondary iron-bearing phases precipitated, yet final dissolved Fe, K, and S concentrations measured in the fluids were non-stoichiometric. The Fe:K and Fe:S molar ratios were several orders of magnitude lower than stoichiometric ratios based on the chemical formula of jarosite, similar to observations made by Welch et al. (2008). This suggests that jarosite dissolution involved preferential removal of potassium and sulfate over iron, similar to observations of non-stoichiometric jarosite dissolution via laboratory experiments and computational modeling (Becker & Gasharova, 2001; Smith et al., 2006). Smith et al. (2006) observed a goethite residue on the surface of jarosite grains after removal of surface K^+ and SO_4^{2-}, but no crystalline secondary iron phases were observed via XRD or VNIR analyses and nanocrystalline or amorphous iron minerals, like ferrihydrite, are unstable at the temperatures of our experiments (Cornell & Schwertmann, 2003). However, the positions of many of the jarosite XRD peaks in the 98 ºC and 200 ºC (Figure 1; Figures S23 and S24) were shifted to different angles compared to the peak positions produced by the initial synthesized jarosite. These shifts better align with the expected diffraction pattern for potassium jarosite and is inconsistent with partial incorporation of H_3O^+ (Basciano & Peterson, 2007; Basciano & Peterson, 2008). Jarosites often contain iron vacancies, leading to an excess of potassium and sulfate in the structure (Scarlett et al., 2010). Heating may have promoted recrystallization that annealed these vacancies, releasing excess K^+ and SO_4^{2-} to solution.

4.1.2 Coarsening of fine-grained, red hematite

The coarsening of finer-grained hematite was minor and did not result in gray hematite. The ~10 nm hematite resulted in a greater relative increase in particle size compared to ~60 nm hematite, which remained largely unchanged in size after 20 days. The increased solubility of smaller particles due to their greater surface area may favor more rapid dissolution and subsequent crystal growth compared to an initially well-crystalline mineral. However, little to no grain size increase was observed for red hematite, regardless of initial crystallite size, suggesting that the coarsening of fine-grained iron oxides alone may not be a viable pathway to gray hematite formation. Minor observed increases in particle size were likely achieved through Ostwald ripening, in which smaller particles are dissolved and reprecipitated as growth onto larger particles (Ostwald, 1897; Steefel & Van Cappellen, 1990). Given unrestricted time in an aqueous environment, finer-grained hematite may eventually coarsen substantially. However, on Mars the duration of aqueous alteration is restricted temporally due to the persistence of diagenetically-juvenile deposits, such as opaline silica and smectites, on the surface (Tosca & Knoll, 2009).

4.1.3 Ferrihydrite and goethite

Ferrihydrite subjected to the same fluid conditions as ~10 nm hematite produced larger grain sizes across all comparable samples despite having a smaller starting crystallite size. The transformation from ferrihydrite to hematite proceeds through the aggregation of smaller particles of ferrihydrite that crystallize to hematite, potentially via a mechanism such as oriented attachment (Freitas et al., 2015; Schwertmann et al., 1999; Soltis et al., 2016; Wang et al., 2022; Zhu & De Yoreo, 2022). Such aggregation-based growth provides a mechanism through which conversion from ferrihydrite generates larger final particles than coarsening of existing ~10 nm hematite. This

410 further highlights the ineffectiveness of Ostwald ripening for generating gray hematite from pre-
411 existing fine-grained hematite.

412 In contrast to the complete conversion of ferrihydrite to hematite, goethite-to-hematite
413 transformation rates were exceedingly slow at 98 ºC, with no hematite formed after 20 days of
414 aging at this temperature. For experiments conducted at 200 ºC, the initial pH of the system
415 dictated the degree of transformation. Acidic systems yield total or near-total transformation of
416 goethite to hematite while 56 to 98% of the goethite remained after aging at pH 7. The relationship
417 between stability at elevated temperature and pH aligns with previous observations (Das et al.,
418 2011; Schwertmann & Carlson, 2005; Smith & Kidd, 1949). Goethite generally produced
419 relatively large (0.2 to 1 μm) particles (Figure 3; Figure S1), but still red hematite except at
420 circumneutral sulfate-rich fluids where little transformation occurred. Consistent with previous
421 observations (Davidson et al., 2008; De Grave et al., 1999; González et al., 2000; Lin et al., 2014),
422 hematite did not retain the acicular form of the precursor goethite. Notably, the bipyramidal
423 morphology of the hematite products (Figure 3; Figure S1) matches that of the hematite formed
424 via epitaxial growth on goethite in hydrothermal systems (Lin et al., 2014), suggesting a
425 dissolution and reprecipitation transformation mechanism.

426 Additional experiments investigating the effects of seeding goethite and ferrihydrite with
427 red, fine-grained hematite to remove possible nucleation barriers resulted in no substantial changes
428 to the transformation products. Seeding also did not affect the final particle sizes of the
429 transformation products. The nucleation rate of hematite therefore does seem to impose a limit on
430 these transformation processes. Particularly with respect to goethite, the inhibition of
431 transformation to hematite under neutral pH conditions at high temperature and all low temperature
432 conditions is not due to a nucleation barrier.

433

434 **4.1.4 Akaganeite and schwertmannite**

435 Unlike jarosite, akaganeite and schwertmannite showed no impact from the common ion
436 effect on their transformations despite containing background salt anions. Akaganeite has been
437 observed to transform to hematite via dissolution and reprecipitation (Bailey et al., 1993; Cornell
438 & Giovanoli, 1990; Goñi-Elizalde et al., 1987; Peterson et al., 2018). The hematite products in this
439 study do not reflect the rod-like morphology of the precursor akageneite and instead appear similar
440 to akageneite transformation products analyzed by Bailey et al. (1993) that formed via dissolution
441 and reprecipitation. This suggests that akageneite in this study transformed to red hematite through
442 a similar mechanism.

443 Schwertmannite displayed a temperature-dependence in is transformation products,
444 forming goethite at 98 °C but red hematite at 200 °C. This is consistent with observations made in
445 prior studies (Barham, 1997; Davidson et al., 2008). These transformations may occur via a
446 ferrihydrite precursor (Davidson et al., 2008), although this cannot be evaluated by our data since
447 no ferrihydrite was detected in the final aging products. Hematite particle sizes (Table 1; Figure 3)
448 were generally larger when produced by a schwertmannite precursor (80 to 130 nm) than for a
449 ferrihydrite precursor (60 to 90 nm). This may reflect the impact of sulfate released during
450 transformation of schwertmannite, differences in pH at the onset of hematite nucleation from a
451 ferrihydrite intermediate, or larger aggregates of ferrihydrite forming in the schwertmannite
452 experiments before crystallization to hematite.

453

454 **4.2 Impacts of initial fluid composition on iron (oxyhydr)oxide transformation products**

455 While each mineral system had variable reaction products and final particle sizes, some
456 general trends were evident across most samples that indicate a specific role of fluid composition.

Experiments in sulfate-rich systems generally resulted in higher final pH values, smaller final particle sizes, and occasionally less complete transformation to hematite. Sulfate commonly adsorbs onto iron oxides as binuclear surface complexes (Hug, 1997; Paul et al., 2005; Wang et al., 2018), which may inhibit the transformation of precursor iron(III) oxides as well as the growth of hematite crystals. Sulfate tends to form binuclear complexes at the surfaces of iron oxides, whereas chloride may bond more weakly (Boily & Shchukarev, 2010; Shchukarev & Boily, 2008; Shchukarev et al., 2007; Shchukarev & Sjöberg, 2005). In contrast, samples in chloride-rich fluids often resulted in complete transformation to hematite, larger final particle sizes, lower final pH values, and higher dissolved iron concentrations. Chloride shows weaker adsorption to iron oxide surfaces than sulfate (Boily & Shchukarev, 2010; Shchukarev & Boily, 2008; Shchukarev et al., 2007; Shchukarev & Sjöberg, 2005) but may promote more rapid dissolution of the precursor phases (Pritchett et al., 2012; Virtanen et al., 1997), potentially increasing the rate of mass transfer to growing hematite crystals. In addition, chloride complexes iron in solution, especially at elevated temperature (Gammons & Allin, 2022; Liu et al., 2006; Stefánsson et al., 2019), increasing the solubility of iron and its availability for hematite growth. The initial pH value also impacts the final fluid composition and reaction products. Experiments initially set to acidic conditions (pH 3) generally resulted in larger final particle sizes, lower final pH values, and more complete transformation to hematite as well, suggesting that acidic conditions may be more favorable to the formation of coarser-grained hematite.

4.3 Jarosite as a potential precursor mineral to gray hematite

Of all the precursor minerals investigated, only jarosite forms hematite of sufficient grain size to be spectrally gray. We hypothesize that this system was uniquely able to maintain both a slow nucleation rate and rapid growth of hematite. Nucleation rate is controlled by the degree of

supersaturation of hematite (De Yoreo & Vekilov, 2003), which depends on the dissolved iron concentration and pH. While jarosite dissolution creates elevated dissolved iron concentrations, it also generates substantial acidity. This apparently prevents the system from reaching high degrees of supersaturation with respect to hematite, creating few nuclei. However, the elevated dissolved iron concentrations enable rapid growth of the small number of nuclei that form, creating large hematite crystallites. The transformation of jarosite to hematite further acidifies the system, creating a positive feedback that drives further jarosite dissolution and hematite growth. Validation of our hypothesized mechanism requires a reactor design that would enable sampling the fluid phase at 200 °C to track the time evolution of dissolved iron and pH.

Incomplete transformation of jarosite to hematite in sulfate-rich fluids may reflect conditions where the phases are in equilibrium. Complete jarosite transformation was only observed in the presence of high dissolve chloride concentration (1 mol L^{-1}), which resulted in over an order of magnitude greater dissolved iron concentration at 200 °C compared to other conditions (Table 3). Complexation of iron(III) sites on the surface of jarosite by chloride may maintain charge balance of the system as sulfate is released and accelerate its dissolution (Pritchett et al., 2012). High concentrations of chloride also form aqueous iron complexes (e.g., $FeCl_4^-$) at elevated temperature (Gammons & Allin, 2022; Liu et al., 2006; Stefánsson et al., 2019), increasing the total concentration of iron in solution. The presence of elevated dissolved chloride in jarosite-bearing systems thus enhances the formation of gray hematite.

In contrast, akaganeite, ferrihydrite, goethite, and schwertmannite may transform through solid-state processes and aggregation of small particles, providing a distinct nucleation route, or generate high degrees of supersaturation while maintaining low dissolved iron concentrations because of the high pH conditions. Further, the iron octahedra in jarosite are corning-sharing (Kato

& Miúra, 1977), but the iron octahedra in hematite are edge and face sharing (Blake et al., 1966; Pauling & Hendricks, 1925). This may slow the initial nucleation of hematite in systems initially containing jarosite. Other iron(III) minerals investigated in this study have edge-sharing octahedra, which may instead facilitate the nucleation of hematite and result in many smaller final hematite particles. Goethite came the closest to generating gray hematite, forming particle at or near 1 μm at 200 ºC. These larger hematite particles may form from goethite via solid-state transformation if its long acicular needles aggregate.

Although this study explores mineral transformations in 98 ºC and 200 ºC fluids, these temperatures were primarily chosen to accelerate the rate of reaction to enable investigation within laboratory time scales. Tosca & Knoll (2009) examined the integration of the temperature and time required to diagenetically transform a given sediment via kinetic formulations. Their models exemplify how mineral transformations have a time-temperature integral threshold that can be met in multiple ways; transformations occurring at lower temperatures over longer periods of time may also occur at higher temperatures much more rapidly. Time-temperature integral thresholds exist for each of the transformations observed in this study; therefore, the results obtained at high (98 ºC and 200 ºC) temperatures over 20 days in this study might also be observed in lower, ambient-temperature aqueous systems over substantially longer time scales. Additionally, while temperature alters chemical equilibria, hematite remains the thermodynamically-stable iron(III) phase at ambient temperatures and above as well as at low water activities (Navrotsky et al., 2008), so this relative stability was not altered by the higher temperatures used.

4.4 Implications for diagenetic hematite at Vera Rubin ridge

Comparison of the results of this investigation with observations by MSL Curiosity provides new insight into the formation conditions of gray, coarse-grained hematite at VRR.

Deposition of VRR and other Murray formation sediments occurred in lacustrine environments (Edgar et al., 2020; Fraeman, Edgar, et al., 2020; Thompson et al., 2020). Much of VRR is red in color, with the isolated gray portions cross-cut strata and laminations indicating a diagenetic origin (Fraeman, Edgar, et al., 2020). Evidence for isochemical alteration at VRR (Bedford et al., 2019) implies that iron in gray, crystalline hematite in the Jura member is derived from pre-existing iron sources in the rocks, such as jarosite. The drill sample Highfield in the gray portion of the Jura member at VRR contained no akaganeite or jarosite while the neighboring drill sites in the red portions of the ridge (Stoer and Rock Hall) contained 1.0 to 2.3 wt.% jarosite and 1.2 to 6.0 wt.% akaganeite (Rampe et al., 2020). The conspicuous absence of jarosite in Highfield is consistent with it having converted to gray hematite via diagenetic alteration. Chloride salts have been confirmed at VRR by evolved gas analyses (EGA) performed by SAM (McAdam et al., 2020), supporting the possibility that chloride-rich fluids were present during diagenesis. While sulfate salts also occur, the presence of calcium sulfate minerals indicate that sulfate solubility would be relatively limited compared to the concentrations used in the present study (0.1 and 1 mol L^{-1}). Calcium sulfate precipitation provides a mechanism to maintain the lower sulfate concentrations that promote jarosite transformation to gray hematite, while similar mechanisms to remove chloride from solution are lacking.

The relative lack of iron in the X-ray amorphous component of VRR sediments compared to the iron content of Duluth (the drill sample in the Blunts Point member just below VRR) may be the result of such phases crystallizing to form iron(III) (oxyhydr)oxides and sulfates such as jarosite, akaganeite, and hematite (McAdam et al., 2020; Rampe et al., 2020). However, it remains unclear whether the amorphous component of VRR sediments could have directly converted to gray, crystalline hematite without first forming an intermediate phase. Jarosite elsewhere in the

Murray formation may be as young as the Amazonian (Martin et al., 2017). If this precursor of gray hematite formed from amorphous material via a prior diagenetic event, then this would indicate multiple periods of aqueous activity that substantially post-dates primary sediment deposition at Gale crater.

The observations of this study further support the formation of gray hematite at VRR as occurring under non-reducing conditions. The isochemical nature of alteration of VRR noted above precludes the formation of gray hematite from Fe(II)-bearing groundwaters because these would have increased the total iron content. Our results provide a formation mechanism for gray hematite that occurs under oxidizing conditions: diagenetic transformation of jarosite. The diagenetic event that produced gray hematite is thus unlikely to have produced a redox gradient that would generate chemical energy to support life at VRR.

5 Conclusions

Jarosite is the first iron(III) mineral known to occur on Mars demonstrated to serve as a diagenetic precursor for gray hematite. Transformation to coarse-grained hematite is aided by acidic conditions generated by jarosite dissolution. This creates low degrees of hematite supersaturation, and thus few initial nuclei, while also maintaining elevated dissolved iron concentrations, leading to fairly rapid particle growth. Chloride-rich fluids, particularly when combined with acidic conditions, appear to play an active role in the dissolution of iron(III) minerals, including jarosite, by increasing precursor mineral dissolution rates and solubilizing iron via aqueous complexation, thereby promoting larger final hematite particle sizes. The gray hematite found throughout VRR may have formed from chloride-rich fluids dissolving jarosite and reprecipitating the iron as hematite. Other minerals investigated (akaganeite, ferrihydrite, goethite, schwertmannite, and fine-grained hematite) are not promising precursor minerals to the

575 gray hematite at VRR. The distinct behavior of jarosite may be due to differences in transformation
576 mechanisms (dissolution and reprecipitation versus solid-state transformation) or slow rates of
577 initial hematite nucleation due to the absence of edge-sharing iron octahedra.
578
579 **Acknowledgements**
580 This research was funded by Washington University. A.L.K. was supported by the NASA
581 Mars Data Analysis Program through Award No. 80NSSC20K0939. K.M. was supported by the
582 NASA Science Mission Directorate Future Investigators in NASA Earth and Space Science and
583 Technology (FINESST) program through Award No. 80NSSC19K1521. J.G.C. was supported by
584 the NASA Exobiology program through Award No. 80NSSC18K1292. Raymond Arvidson, Paul
585 Carpenter, and Elaine Flynn are thanked for their assistance with sample characterization. The
586 authors acknowledge support from the Institute of Materials Science and Engineering for the use
587 of laboratory instruments and staff assistance.
588
589 **Open Research**
590 All data used in the manuscript are available in the supporting information or in
591 Washington University in St. Louis Research Data via https://doi.org/10.7936/6rxs-103632 with
592 Creative Commons Attribution (CC BY) 4.0 International (Knight et al., 2023). Profex version 5
593 used for refinement of X-ray diffraction patterns is preserved at https://www.profex-xrd.org/
594 (Doebelin & Kleeberg, 2015). ImageJ version 1.53k used for grain size analyses is preserved at
595 https://imagej.nih.gov/ij/download.html (Schneider et al., 2012).
596
597
598

References

Bailey, J. K., Brinker, C. J., & Mecartney, M. L. (1993). Growth mechanisms of iron oxide particles of differing morphologies from the forced hydrolysis of ferric chloride solutions. *Journal of Colloid and Interface Science*, *157*(1), 1-13. https://doi.org/10.1006/jcis.1993.1150

Barham, R. J. (1997). Schwertmannite: A unique mineral, contains a replaceable ligand, transforms to jarosites, hematites, and/or basic iron sulfate. *Journal of Materials Research*, *12*(10), 2751-2758. https://doi.org/10.1557/JMR.1997.0366

Basciano, L. C., & Peterson, R. C. (2007). Jarosite–hydronium jarosite solid-solution series with full iron site occupancy: Mineralogy and crystal chemistry. *American Mineralogist*, *92*(8-9), 1464-1473. https://doi.org/10.2138/am.2007.2432

Basciano, L. C., & Peterson, R. C. (2008). Crystal chemistry of the natrojarosite-jarosite and natrojarosite-hydronium jarosite solid-solution series: A synthetic study with full Fe site occupancy. *American Mineralogist*, *93*(5-6), 853-862. https://doi.org/10.2138/am.2008.2731

Becker, U., & Gasharova, B. (2001). AFM observations and simulations of jarosite growth at the molecular scale: Probing the basis for the incorporation of foreign ions into jarosite as a storage mineral. *Physics and Chemistry of Minerals*, *28*(8), 545-556. https://doi.org/10.1007/s002690100188

Bedford, C. C., Bridges, J. C., Schwenzer, S. P., Wiens, R. C., Rampe, E. B., Frydenvang, J., & Gasda, P. J. (2019). Alteration trends and geochemical source region characteristics preserved in the fluviolacustrine sedimentary record of Gale crater, Mars. *Geochimica et Cosmochimica Acta*, *246*, 234-266. https://doi.org/10.1016/j.gca.2018.11.031

622 Bennett, K. A., Rivera-Hernández, F., Tinker, C., Horgan, B., Fey, D. M., Edwards, C., Edgar, L.
623 A., Kronyak, R., Edgett, K. S., Fraeman, A., Kah, L. C., Henderson, M., Stein, N.,
624 Dehouck, E., & Williams, A. J. (2021). Diagenesis Revealed by Fine-Scale Features at
625 Vera Rubin Ridge, Gale Crater, Mars. *Journal of Geophysical Research: Planets*, *126*(5),
626 e2019JE006311. https://doi.org/10.1029/2019JE006311
627 Blake, R. L., Hessevick, R. E., Zoltai, T., & Finger, L. W. (1966). Refinement of the hematite
628 structure. *American Mineralogist*, *51*(1-2), 123-129.
629 Boily, J.-F., & Shchukarev, A. (2010). X-ray Photoelectron Spectroscopy of Fast-Frozen
630 Hematite Colloids in Aqueous Solutions. 2. Tracing the Relationship between Surface
631 Charge and Electrolyte Adsorption. *The Journal of Physical Chemistry C*, *114*(6), 2613-
632 2616. https://doi.org/10.1021/jp908197f
633 Catling, D. C., & Moore, J. M. (2003). The nature of coarse-grained crystalline hematite and its
634 implications for the early environment of Mars. *Icarus*, *165*(2), 277-300.
635 https://doi.org/10.1016/S0019-1035(03)00173-8
636 Christensen, P. R., Morris, R. V., Lane, M. D., Bandfield, J. L., & Malin, M. C. (2001). Global
637 mapping of Martian hematite mineral deposits: Remnants of water-driven processes on
638 early Mars. *Journal of Geophysical Research: Planets*, *106*(E10), 23873-23885.
639 https://doi.org/10.1029/2000je001415
640 Clark, J. V., Sutter, B., McAdam, A. C., Rampe, E. B., Archer, P. D., Ming, D. W., Navarro-
641 Gonzalez, R., Mahaffy, P., & Lapen, T. J. (2020). High-temperature HCl evolutions from
642 mixtures of perchlorates and chlorides with water-bearing phases: Implications for the
643 SAM instrument in Gale crater, Mars. *Journal of Geophysical Research: Planets*, *125*(2),
644 e2019JE006173. https://doi.org/10.1029/2019JE006173

645 Cornell, R. M., & Giovanoli, R. (1990). Transformation of akaganéite into goethite and hematite
646 in alkaline media. *Clays and Clay Minerals*, *38*(5), 469-476.
647 https://doi.org/10.1346/CCMN.1990.0380502
648 Cornell, R. M., & Schwertmann, U. (2003). *The iron oxides: Structure, properties, reactions,*
649 *occurences and uses*. Weinheim: John Wiley & Sons.
650 Das, S., Hendry, M., & Essilfie-Dughan, J. (2011). Transformation of two-line ferrihydrite to
651 goethite and hematite as a function of pH and temperature. *Environmental Science &*
652 *Technology*, *45*, 268-75. https://doi.org/10.1021/es101903y
653 Davidson, L. E., Shaw, S., & Benning, L. G. (2008). The kinetics and mechanisms of
654 schwertmannite transformation to goethite and hematite under alkaline conditions.
655 *American Mineralogist*, *93*(8-9), 1326-1337. https://doi.org/10.2138/am.2008.2761
656 De Grave, E., Vochten, R., Quenard, O., Van San, E., Desseyn, H., & Rousset, A. (1999).
657 Mössbauer characterisation of the products resulting from hydrothermal treatments of
658 nanosized goethite. *Nanostructured Materials*, *11*(4), 493-504.
659 https://doi.org/10.1016/s0965-9773(99)00334-7
660 De Yoreo, J. J., & Vekilov, P. G. (2003). Principles of Crystal Nucleation and Growth. *Reviews*
661 *in Mineralogy and Geochemistry*, *54*(1), 57-93. https://doi.org/10.2113/0540057
662 Doebelin, N., & Kleeberg, R. (2015). Profex: A graphical user interface for the Rietveld
663 refinement program BGMN. *Journal of Applied Crystallography*, *48*(5), 1573-1580.
664 https://doi.org/10.1107/s1600576715014685
665 Edgar, L. A., Fedo, C. M., Gupta, S., Banham, S. G., Fraeman, A. A., Grotzinger, J. P., Stack, K.
666 M., Stein, N. T., Bennett, K. A., Rivera-Hernández, F., Sun, V. Z., Edgett, K. S., Rubin,
667 D. M., House, C., & Van Beek, J. (2020). A lacustrine paleoenvironment recorded at

668 Vera Rubin ridge, Gale crater: Overview of the sedimentology and stratigraphy observed
669 by the Mars Science Laboratory Curiosity rover. *Journal of Geophysical Research:*
670 *Planets*, *125*(3), e2019JE006307. https://doi.org/10.1029/2019JE006307
671 Egami, T., & Billinge, S. (2012). *Underneath the Bragg peaks: Structural analysis of complex*
672 *materials*, 16. Amsterdam, The Netherlands: Permagon.
673 Fallacaro, A., & Calvin, W. M. (2006). Spectral Properties of Lake Superior Banded Iron
674 Formation: Application to Martian Hematite Deposits. *Astrobiology*, *6*(4), 563-580.
675 https://doi.org/10.1089/ast.2006.6.563
676 Fraeman, A. A., Arvidson, R. E., Catalano, J. G., Grotzinger, J. P., Morris, R. V., Murchie, S. L.,
677 Stack, K. M., Humm, D. C., McGovern, J. A., Seelos, F. P., Seelos, K. D., & Viviano, C.
678 E. (2013). A hematite-bearing layer in Gale Crater, Mars: Mapping and implications for
679 past aqueous conditions. *Geology*, *41*(10), 1103-1106. https://doi.org/10.1130/g34613.1
680 Fraeman, A. A., Edgar, L. A., Rampe, E. B., Thompson, L. M., Frydenvang, J., Fedo, C. M.,
681 Catalano, J. G., Dietrich, W. E., Gabriel, T. S. J., Grotzinger, J. P., L'Haridon, J.,
682 Mangold, N., Sun, V. Z., House, C. H., Bryk, A., Hardgrove, C., Czarnecki, S., Stack, K.
683 M., Morris, R. V., Arvidson, R. E., Banham, S. G., Bennett, K. A., Bridges, J. C.,
684 Edwards, C. S., Fischer, W. W., Fox, V. K., Gupta, S., Horgan, B. H. N., Jacob, S. R.,
685 Johnson, J. R., Johnson, S. S., Rubin, D. R., Salvatore, M. R., Schwenzer, S. P., Siebach,
686 K. L., Stein, N. T., Turner, S., Wellington, D. F., Wiens, R. C., Williams, A. J.,
687 Davidson, G. A., & Wong, G. M. (2020). Evidence for a diagenetic origin of Vera Rubin
688 Ridge, Gale Crater, Mars: Summary and synthesis of Curiosity's exploration campaign.
689 *Journal of Geophysical Research: Planets*, *125*(12), e2020JE006527.
690 https://doi.org/10.1029/2020JE006527

691 Fraeman, A. A., Ehlmann, B. L., Arvidson, R. E., Edwards, C. S., Grotzinger, J. P., Milliken, R.
692 E., Quinn, D. P., & Rice, M. S. (2016). The stratigraphy and evolution of lower Mount
693 Sharp from spectral, morphological, and thermophysical orbital data sets. *Journal of*
694 *Geophysical Research: Planets*, *121*(9), 1713-1736.
695 https://doi.org/10.1002/2016JE005095
696 Fraeman, A. A., Johnson, J. R., Arvidson, R. E., Rice, M. S., Wellington, D. F., Morris, R. V.,
697 Fox, V. K., Horgan, B. H. N., Jacob, S. R., Salvatore, M. R., Sun, V. Z., Pinet, P., Bell, J.
698 F., Wiens, R. C., & Vasavada, A. R. (2020). Synergistic ground and orbital observations
699 of iron oxides on Mt. Sharp and Vera Rubin ridge. *Journal of Geophysical Research:*
700 *Planets*, *125*(9), e2019JE006294. https://doi.org/10.1029/2019je006294
701 Freitas, E. T. F., Montoro, L. A., Gasparon, M., & Ciminelli, V. S. T. (2015). Natural attenuation
702 of arsenic in the environment by immobilization in nanostructured hematite.
703 *Chemosphere*, *138*, 340-347. https://doi.org/10.1016/j.chemosphere.2015.05.101
704 Frydenvang, J., Gasda, P. J., Hurowitz, J. A., Grotzinger, J. P., Wiens, R. C., Newsom, H. E.,
705 Edgett, K. S., Watkins, J., Bridges, J. C., Maurice, S., Fisk, M. R., Johnson, J. R., Rapin,
706 W., Stein, N. T., Clegg, S. M., Schwenzer, S. P., Bedford, C. C., Edwards, P., Mangold,
707 N., Cousin, A., Anderson, R. B., Payré, V., Vaniman, D., Blake, D. F., Lanza, N. L.,
708 Gupta, S., Van Beek, J., Sautter, V., Meslin, P. Y., Rice, M., Milliken, R., Gellert, R.,
709 Thompson, L., Clark, B. C., Sumner, D. Y., Fraeman, A. A., Kinch, K. M., Madsen, M.
710 B., Mitrofanov, I. G., Jun, I., Calef, F., & Vasavada, A. R. (2017). Diagenetic silica
711 enrichment and late-stage groundwater activity in Gale crater, Mars. *Geophysical*
712 *Research Letters*, *44*(10), 4716-4724. https://doi.org/10.1002/2017GL073323

713 Gammons, C. H., & Allin, N. C. (2022). Stability of aqueous Fe(III) chloride complexes and the
714 solubility of hematite between 150 and 300 °C. *Geochimica et Cosmochimica Acta*, *330*,
715 148-164. https://doi.org/10.1016/j.gca.2021.01.043
716 Golden, D. C., Ming, D. W., Morris, R. V., & Graff, T. G. (2008). Hydrothermal synthesis of
717 hematite spherules and jarosite: Implications for diagenesis and hematite spherule
718 formation in sulfate outcrops at Meridiani Planum, Mars. *American Mineralogist*, *93*(8-
719 9), 1201-1214. https://doi.org/10.2138/am.2008.2737
720 Goñi-Elizalde, S., Garcia-Clavel, M. E., & Tejedor-Tejedor, M. I. (1987). Mechanism of
721 akaganeite-hematite transformation via solution. *Reactivity of Solids*, *3*(1), 139-154.
722 https://doi.org/10.1016/0168-7336(87)80024-4
723 González, G., Sagarzazu, A., & Villalba, R. (2000). Study of the mechano-chemical
724 transformation of goethite to hematite by TEM and XRD. *Materials Research Bulletin*,
725 *35*(14), 2295-2308. https://doi.org/10.1016/S0025-5408(00)00434-7
726 Horgan, B. H. N., Johnson, J. R., Fraeman, A. A., Rice, M. S., Seeger, C., Bell III, J. F., Bennett,
727 K. A., Cloutis, E. A., Edgar, L. A., Frydenvang, J., Grotzinger, J. P., L'Haridon, J., Jacob,
728 S. R., Mangold, N., Rampe, E. B., Rivera-Hernandez, F., Sun, V. Z., Thompson, L. M., &
729 Wellington, D. (2020). Diagenesis of Vera Rubin ridge, Gale crater, Mars, from Mastcam
730 multispectral images. *Journal of Geophysical Research: Planets*, *125*(11),
731 e2019JE006322. https://doi.org/10.1029/2019JE006322
732 Hug, S. J. (1997). In situ Fourier transform infrared measurements of sulfate adsorption on
733 hematite in aqueous solutions. *Journal of Colloid and Interface Science*, *188*(2), 415-422.
734 https://doi.org/10.1006/jcis.1996.4755

735 Janney, D. E., Cowley, J. M., & Buseck, P. R. (2000). Transmission electron microscopy of
736 synthetic 2- and 6-line ferrihydrite. *Clays and Clay Minerals*, *48*(1), 111-119.
737 https://doi.org/10.1346/ccmn.2000.0480114
738 Jensen, J. L., Siddoway, C. S., Reiners, P. W., Ault, A. K., Thomson, S. N., & Steele-MacInnis,
739 M. (2018). Single-crystal hematite (U–Th)/He dates and fluid inclusions document
740 widespread Cryogenian sand injection in crystalline basement. *Earth and Planetary*
741 *Science Letters*, *500*, 145-155. https://doi.org/10.1016/j.epsl.2018.08.021
742 Johnson, J. R., Bell, J. F., III, Bender, S., Blaney, D., Cloutis, E., Ehlmann, B., Fraeman, A.,
743 Gasnault, O., Kinch, K., Le Mouélic, S., Maurice, S., Rampe, E., Vaniman, D., & Wiens,
744 R. C. (2016). Constraints on iron sulfate and iron oxide mineralogy from ChemCam
745 visible/near-infrared reflectance spectroscopy of Mt. Sharp basal units, Gale Crater,
746 Mars. *American Mineralogist*, *101*(7), 1501-1514. https://doi.org/10.2138/am-2016-5553
747 Kato, T., & Miúra, Y. (1977). The crystal structures of jarosite and svanbergite. *Mineralogical*
748 *Journal*, *8*(8), 419-430.
749 Kerker, M., Scheiner, P., Cooke, D. D., & Kratohvil, J. P. (1979). Absorption index and color of
750 colloidal hematite. *Journal of Colloid and Interface Science*, *71*(1), 176-187.
751 https://doi.org/10.1016/0021-9797(79)90231-5
752 Knight, A. L., Mitra, K., & Catalano, J. G. (2023). Mineral products and fluid compositions from
753 the transformations of iron(III) minerals in Mars-relevant fluids (Version 1) [Dataset].
754 Washington University in St. Louis Research Data. https://doi.org/10.7936/6rxs-103632
755 Lane, M. D., Morris, R. V., Mertzman, S. A., & Christensen, P. R. (2002). Evidence for platy
756 hematite grains in Sinus Meridiani, Mars. *Journal of Geophysical Research: Planets*,
757 *107*(E12), 5126. https://doi.org/10.1029/2001je001832

758 Lin, M., Tng, L., Lim, T., Choo, M., Zhang, J., Tan, H. R., & Bai, S. (2014). Hydrothermal
759 synthesis of octadecahedral hematite (α-Fe_2O_3) nanoparticles: An epitaxial growth from
760 goethite (α-FeOOH). *The Journal of Physical Chemistry C*, *118*(20), 10903-10910.
761 https://doi.org/10.1021/jp502087h
762 Liu, W., Etschmann, B., Brugger, J., Spiccia, L., Foran, G., & McInnes, B. (2006). UV–Vis
763 spectrophotometric and XAFS studies of ferric chloride complexes in hyper-saline LiCl
764 solutions at 25–90 °C. *Chemical Geology*, *231*(4), 326-349.
765 https://doi.org/10.1016/j.chemgeo.2006.02.005
766 Martin, P. E., Farley, K. A., Baker, M. B., Malespin, C. A., Schwenzer, S. P., Cohen, B. A.,
767 Mahaffy, P. R., McAdam, A. C., Ming, D. W., Vasconcelos, P. M., & Navarro-González,
768 R. (2017). A two-step K-Ar experiment on Mars: Dating the diagenetic formation of
769 jarosite from Amazonian groundwaters. *Journal of Geophysical Research: Planets*,
770 *122*(12), 2803-2818. https://doi.org/10.1002/2017JE005445
771 McAdam, A. C., Sutter, B., Archer, P. D., Franz, H. B., Wong, G. M., Lewis, J. M. T.,
772 Eigenbrode, J. L., Stern, J. C., Knudson, C. A., Clark, J. V., Andrejkovičová, S., Ming, D.
773 W., Morris, R. V., Achilles, C. N., Rampe, E. B., Bristow, T. F., Navarro-González, R.,
774 Mahaffy, P. R., Thompson, L. M., Gellert, R., Williams, A. J., House, C. H., & Johnson,
775 S. S. (2020). Constraints on the mineralogy and geochemistry of Vera Rubin ridge, Gale
776 crater, Mars, from Mars Science Laboratory Sample Analysis at Mars Evolved Gas
777 Analyses. *Journal of Geophysical Research: Planets*, *125*(11), e2019JE006309.
778 https://doi.org/10.1029/2019JE006309
779 Michel, F. M., Ehm, L., Liu, G., Han, W. Q., Antao, S. M., Chupas, P. J., Lee, P. L., Knorr, K.,
780 Eulert, H., Kim, J., Grey, C. P., Celestian, A. J., Gillow, J., Schoonen, M. A. A.,

781 Strongin, D. R., & Parise, J. B. (2007). Similarities in 2- and 6-line ferrihydrite based on
782 pair distribution function analysis of X-ray total scattering. *Chemistry of Materials*, *19*(6),
783 1489-1496. https://doi.org/10.1021/cm062585n
784 Morris, R. V., Golden, D. C., Bell, J. F., Shelfer, T. D., Scheinost, A. C., Hinman, N. W.,
785 Furniss, G., Mertzman, S. A., Bishop, J. L., Ming, D. W., Allen, C. C., & Britt, D. T.
786 (2000). Mineralogy, composition, and alteration of Mars Pathfinder rocks and soils:
787 Evidence from multispectral, elemental, and magnetic data on terrestrial analogue, SNC
788 meteorite, and Pathfinder samples. *Journal of Geophysical Research: Planets*, *105*(E1),
789 1757-1817. https://doi.org/10.1029/1999je001059
790 Morris, R. V., Rampe, E. B., Vaniman, D. T., Christoffersen, R., Yen, A. S., Morrison, S. M.,
791 Ming, D. W., Achilles, C. N., Fraeman, A. A., Le, L., Tu, V. M., Ott, J. P., Treiman, A.
792 H., Hogancamp, J. V., Graff, T. G., Adams, M., Hamilton, J. C., Mertzman, S. A.,
793 Bristow, T. F., Blake, D. F., Castle, N., Chipera, S. J., Craig, P. I., Des Marais, D. J.,
794 Downs, G., Downs, R. T., Hazen, R. M., Morookian, J.-M., & Thorpe, M. (2020).
795 Hydrothermal precipitation of sanidine (adularia) having full Al,Si structural disorder and
796 specular hematite at Maunakea Volcano (Hawai'i) and at Gale crater (Mars). *Journal of*
797 *Geophysical Research: Planets*, *125*(9), e2019JE006324.
798 https://doi.org/10.1029/2019JE006324
799 Navrotsky, A., Mazeina, L., & Majzlan, J. (2008). Size-driven structural and thermodynamic
800 complexity in iron oxides. *Science*, *319*(5870), 1635-1638.
801 https://doi.org/10.1126/science.1148614

802 Ostwald, W. (1897). Studien über die Bildung und Umwandlung fester Körper: 1. Abhandlung:
803 Übersättigung und Überkaltung. *Zeitschrift für Physikalische Chemie*, *22U*(1), 289-330.
804 https://doi.org/10.1515/zpch-1897-2233
805 Paul, K. W., Borda, M. J., Kubicki, J. D., & Sparks, D. L. (2005). Effect of Dehydration on
806 Sulfate Coordination and Speciation at the Fe−(Hydr)oxide−Water Interface: A
807 Molecular Orbital/Density Functional Theory and Fourier Transform Infrared
808 Spectroscopic Investigation. *Langmuir*, *21*(24), 11071-11078.
809 https://doi.org/10.1021/la050648v
810 Pauling, L., & Hendricks, S. B. (1925). The crystal structures of hematite and corundum. *Journal*
811 *of the American Chemical Society*, *47*(3), 781-790. https://doi.org/10.1021/ja01680a027
812 Peterson, K. M., Heaney, P. J., & Post, J. E. (2018). Evolution in the structure of akaganeite and
813 hematite during hydrothermal growth: An in situ synchrotron X-ray diffraction analysis.
814 *Powder Diffraction*, *33*(4), 287-297. https://doi.org/10.1017/S0885715618000623
815 Pritchett, B. N., Elwood Madden, M. E., & Madden, A. S. (2012). Jarosite dissolution rates and
816 maximum lifetimes in high salinity brines: Implications for Earth and Mars. *Earth and*
817 *Planetary Science Letters*, *357-358*, 327-336. https://doi.org/10.1016/j.epsl.2012.09.011
818 Rampe, E. B., Bristow, T. F., Morris, R. V., Morrison, S. M., Achilles, C. N., Ming, D. W.,
819 Vaniman, D. T., Blake, D. F., Tu, V. M., Chipera, S. J., Yen, A. S., Peretyazhko, T. S.,
820 Downs, R. T., Hazen, R. M., Treiman, A. H., Grotzinger, J. P., Castle, N., Craig, P. I.,
821 Des Marais, D. J., Thorpe, M. T., Walroth, R. C., Downs, G. W., Fraeman, A. A.,
822 Siebach, K. L., Gellert, R., Lafuente, B., McAdam, A. C., Meslin, P. Y., Sutter, B., &
823 Salvatore, M. R. (2020). Mineralogy of Vera Rubin ridge from the Mars Science

824 Laboratory CheMin instrument. *Journal of Geophysical Research: Planets*, *125*(9).
825 https://doi.org/10.1029/2019je006306
826 Scarlett, N. V. Y., Grey, I. E., & Brand, H. E. A. (2010). Ordering of iron vacancies in
827 monoclinic jarosites. *American Mineralogist*, *95*(10), 1590-1593.
828 https://doi.org/10.2138/am.2010.3591
829 Schneider, C. A., Rasband, W. S., & Eliceiri, K. W. (2012). NIH Image to ImageJ: 25 years of
830 image analysis. *Nature Methods*, *9*(7), 671-675. https://doi.org/10.1038/nmeth.2089
831 Schwertmann, U., & Carlson, L. (2005). The pH-dependent transformation of schwertmannite to
832 goethite at 25°C. *Clay Minerals*, *40*(1), 63-66.
833 https://doi.org/10.1180/0009855054010155
834 Schwertmann, U., Friedl, J., & Stanjek, H. (1999). From Fe(III) ions to ferrihydrite and then to
835 hematite. *Journal of Colloid and Interface Science*, *209*(1), 215-223.
836 https://doi.org/10.1006/jcis.1998.5899
837 Shchukarev, A., & Boily, J.-F. (2008). XPS study of the hematite–aqueous solution interface.
838 *Surface and Interface Analysis*, *40*(3-4), 349-353. https://doi.org/10.1002/sia.2657
839 Shchukarev, A., Boily, J.-F., & Felmy, A. R. (2007). XPS of Fast-Frozen Hematite Colloids in
840 NaCl Aqueous Solutions: I. Evidence for the Formation of Multiple Layers of Hydrated
841 Sodium and Chloride Ions Induced by the {001} Basal Plane. *The Journal of Physical*
842 *Chemistry C*, *111*(49), 18307-18316. https://doi.org/10.1021/jp075321c
843 Shchukarev, A., & Sjöberg, S. (2005). XPS with fast-frozen samples: A renewed approach to
844 study the real mineral/solution interface. *Surface Science*, *584*(1), 106-112.
845 https://doi.org/10.1016/j.susc.2005.01.060

Sherman, D. M. (1985). The electronic structures of Fe^{3+} coordination sites in iron oxides: Applications to spectra, bonding, and magnetism. *Physics and Chemistry of Minerals*, *12*(3), 161-175. https://doi.org/10.1007/bf00308210

Sherman, D. M., & Waite, T. D. (1985). Electronic spectra of Fe^{3+} oxides and oxide hydroxides in the near IR to near UV. *American Mineralogist*, *70*, 1262-1269.

Smith, A. M. L., Hudson-Edwards, K. A., Dubbin, W. E., & Wright, K. (2006). Dissolution of jarosite [$KFe_3(SO_4)_2(OH)_6$] at pH 2 and 8: Insights from batch experiments and computational modelling. *Geochimica et Cosmochimica Acta*, *70*(3), 608-621. https://doi.org/10.1016/j.gca.2005.09.024

Smith, F. G., & Kidd, D. J. (1949). Hematite-goethite relations in neutral and alkaline solutions under pressure. *American Mineralogist*, *34*(5-6), 403-412.

Soltis, J. A., Feinberg, J. M., Gilbert, B., & Penn, R. L. (2016). Phase Transformation and Particle-Mediated Growth in the Formation of Hematite from 2-Line Ferrihydrite. *Crystal Growth & Design*, *16*(2), 922-932. https://doi.org/10.1021/acs.cgd.5b01471

Stack, K. M., Grotzinger, J. P., Kah, L. C., Schmidt, M. E., Mangold, N., Edgett, K. S., Sumner, D. Y., Siebach, K. L., Nachon, M., Lee, R., Blaney, D. L., Deflores, L. P., Edgar, L. A., Fairén, A. G., Leshin, L. A., Maurice, S., Oehler, D. Z., Rice, M. S., & Wiens, R. C. (2014). Diagenetic origin of nodules in the Sheepbed member, Yellowknife Bay formation, Gale crater, Mars. *Journal of Geophysical Research: Planets*, *119*(7), 1637-1664. https://doi.org/10.1002/2014je004617

Steefel, C. I., & Van Cappellen, P. (1990). A new kinetic approach to modeling water-rock interaction: The role of nucleation, precursors, and Ostwald ripening. *Geochimica et Cosmochimica Acta*, *54*(10), 2657-2677. https://doi.org/10.1016/0016-7037(90)90003-4

869 Stefánsson, A., Lemke, K. H., & Seward, T. M. (2019). Iron(III) chloride complexation in
870 hydrothermal solutions: A combined spectrophotometric and density functional theory
871 study. *Chemical Geology*, *524*, 77-87. https://doi.org/10.1016/j.chemgeo.2019.05.039
872 Thomas, N. H., Ehlmann, B. L., Rapin, W., Rivera-Hernández, F., Stein, N. T., Frydenvang, J.,
873 Gabriel, T., Meslin, P.-Y., Maurice, S., & Wiens, R. C. (2020). Hydrogen variability in
874 the Murray formation, Gale crater, Mars. *Journal of Geophysical Research: Planets*,
875 *125*(9), e2019JE006289. https://doi.org/10.1029/2019JE006289
876 Thompson, L. M., Berger, J. A., Spray, J. G., Fraeman, A. A., McCraig, M. A., O'Connell-
877 Cooper, C. D., Schmidt, M. E., Vanbommel, S., Gellert, R., Yen, A., & Boyd, N. I.
878 (2020). APXS-derived compositional characteristics of Vera Rubin ridge and Murray
879 formation, Gale crater, Mars: Geochemical implications for the origin of the ridge.
880 *Journal of Geophysical Research: Planets*, *125*(10).
881 https://dx.doi.org/10.1029/2019je006319
882 Thomson, B. J., Bridges, N. T., Milliken, R., Baldridge, A., Hook, S. J., Crowley, J. K., Marion,
883 G. M., de Souza Filho, C. R., Brown, A. J., & Weitz, C. M. (2011). Constraints on the
884 origin and evolution of the layered mound in Gale Crater, Mars using Mars
885 Reconnaissance Orbiter data. *Icarus*, *214*(2), 413-432.
886 https://doi.org/10.1016/j.icarus.2011.05.002
887 Tosca, N. J., & Knoll, A. H. (2009). Juvenile chemical sediments and the long term persistence
888 of water at the surface of Mars. *Earth and Planetary Science Letters*, *286*(3-4), 379-386.
889 https://doi.org/10.1016/j.epsl.2009.07.004
890 Virtanen, S., Schmuki, P., Davenport, A. J., & Vitus, C. M. (1997). Dissolution of thin iron oxide
891 films used as models for iron passive films studied by in situ X-ray absorption near-edge

spectroscopy. *Journal of the Electrochemical Society*, *144*(1), 198. https://doi.org/10.1149/1.1837385

Wang, X., Wang, Z., Peak, D., Tang, Y., Feng, X., & Zhu, M. (2018). Quantification of coexisting inner- and outer-sphere complexation of sulfate on hematite surfaces. *ACS Earth and Space Chemistry*, *2*(4), 387-398. https://doi.org/10.1021/acsearthspacechem.7b00154

Wang, Y., Xue, S., Lin, Q., Song, D., He, Y., Liu, L., Zhou, J., Zong, M., De Yoreo, J. J., Zhu, J., Rosso, K. M., Sushko, M. L., & Zhang, X. (2022). Particle-based hematite crystallization is invariant to initial particle morphology. *Proceedings of the National Academy of Sciences*, *119*(11). https://dx.doi.org/10.1073/pnas.2112679119

Welch, S. A., Kirste, D., Christy, A. G., Beavis, F. R., & Beavis, S. G. (2008). Jarosite dissolution II—Reaction kinetics, stoichiometry and acid flux. *Chemical Geology*, *254*(1), 73-86. https://doi.org/10.1016/j.chemgeo.2008.06.010

Yen, A., Morris, R. V., Ming, D. W., Schwenzer, S. P., Sutter, B., Vaniman, D., Treiman, A. H., Gellert, R., Achilles, C., & Berger, J. (2021). Formation of tridymite and evidence for a hydrothermal history at gale crater, Mars. *Journal of Geophysical Research: Planets*, *126*(3), e2020JE006569.

Zhu, G., & De Yoreo, J. J. (2022). Hematite Crystallization from a Two-Line Ferrihydrite Suspension. *Journal of The Electrochemical Society*, *169*(10), 102510. https://dx.doi.org/10.1149/1945-7111/ac99a0

References From the Supporting Information

914 Baron, D., & Palmer, C. D. (1996). Solubility of jarosite at 4–35 °C. *Geochimica et*
915 *Cosmochimica Acta*, *60*(2), 185-195. https://doi.org/10.1016/0016-7037(95)00392-4
916 Madden, A. S., & Hochella, M. F. (2005). A test of geochemical reactivity as a function of
917 mineral size: Manganese oxidation promoted by hematite nanoparticles. *Geochimica et*
918 *Cosmochimica Acta*, *69*(2), 389-398. https://doi.org/10.1016/j.gca.2004.06.035
919 Mulvaney, P., Cooper, R., Grieser, F., & Meisel, D. (1988). Charge trapping in the reductive
920 dissolution of colloidal suspensions of iron(III) oxides. *Langmuir*, *4*(5), 1206-1211.
921 https://doi.org/10.1021/la00083a028
922 Schwertmann, U., & Cornell, R. M. (2000). *Iron oxides in the laboratory: Preparation and*
923 *characterization*. Weinheim: John Wiley & Sons.
924
925